

# Image Restoration via Multi-domain Learning

Xingyu Jiang, Ning Gao, Xiuhui Zhang, Hongkun Dou, Shaowen Fu, Xiaoqing Zhong, Hongjue Li and Yue Deng, *Senior Member, IEEE*,

**Abstract**—Due to adverse atmospheric and imaging conditions, natural images suffer from various degradation phenomena. Consequently, image restoration has emerged as a key solution and garnered substantial attention. Although recent Transformer architectures have demonstrated impressive success across various restoration tasks, their considerable model complexity poses significant challenges for both training and real-time deployment. Furthermore, instead of investigating the commonalities among different degradations, most existing restoration methods focus on modifying Transformer under limited restoration priors. In this work, we first review various degradation phenomena under multi-domain perspective, identifying common priors. Then, we introduce a novel restoration framework, which integrates multi-domain learning into Transformer. Specifically, in Token Mixer, we propose a Spatial-Wavelet-Fourier multi-domain structure that facilitates local-region-global multi-receptive field modeling to replace vanilla self-attention. Additionally, in Feed-Forward Network, we incorporate multi-scale learning to fuse multi-domain features at different resolutions. Comprehensive experimental results across ten restoration tasks, such as dehazing, desnowing, motion deblurring, defocus deblurring, rain streak/raindrop removal, cloud removal, shadow removal, underwater enhancement and low-light enhancement, demonstrate that our proposed model outperforms state-of-the-art methods and achieves a favorable trade-off among restoration performance, parameter size, computational cost and inference latency. The code is available at: <https://github.com/deng-ai-lab/SWFormer>.

**Index Terms**—Image Restoration, Image Enhancement, Global Modeling, Spatial-Wavelet-Fourier Multi-domain Learning.

## I. INTRODUCTION

NATURAL images can suffer from various degradation processes (as shown in Fig.1(a)), resulting from atmospheric scattering effects (e.g., dehazing [36], remote sensing cloud removal [60], underwater enhancement [51]), dynamic medium interference (e.g., rain streak/rain drop removal [71], [97], snow removal [62]), optical system imperfections (e.g., defocus blur removal [2], motion blur removal [66]) and lighting condition limitations (e.g., low-light enhancement [6], shadow removal [34]). These degradations lead to significant reductions in image contrast, color shift and geometric distortions, which severely affect image quality assessment and hinder the performance of downstream visual tasks [40], [107]. To this end, image restoration has emerged as a key solution, with the goal of reconstructing high-quality clear images from low-quality degraded inputs, and has garnered extensive attention in the computer vision community over the past few decades. However, due to the inherently ill-posed nature of restoration problem, designing an efficient model capable of effectively handling various degradation tasks remains a

highly complex challenge. So far, current image restoration techniques can generally be classified into two categories: prior-based methods [36], [100] and data-driven methods [31], [43]. Prior-based models treat image restoration as an ill-posed optimization problem, incorporating physical priors to constrain the solution space, but may struggle in complex, real-world scenarios. In contrast, data-driven models, particularly convolutional neural networks (CNNs), employ an end-to-end manner to solve image restoration and have achieved successful breakthroughs. More recently, Transformer-like self-attention approaches [12], [103] have emerged and delivered state-of-the-art (SOTA) performance across various tasks.

Despite the significant progress made by Transformer-like approaches in image restoration, the accompanying increase in model complexity presents substantial challenges for both training and real-time deployment. To address this problem, existing restoration methods have attempted to optimize the Transformer architecture. For instance, Restormer [103] introduces channel self-attention, GRL [54] incorporates anchor self-attention and DRSformer [12] adopts sparse self-attention to reduce model complexity. However, these approaches overlook the common priors across different degradation processes in network design, failing to effectively integrate the inherent characteristics of restoration tasks themselves. With limited restoration priors, existing methods struggle to achieve an optimal balance among performance, parameter size, computational cost and inference latency. In Fig.1(b), DRSformer [12] approach has  $\times 35$  more parameters,  $\times 12$  more computational cost and  $\times 6.8$  longer inference latency than our SWFormer-s, yet its average PSNR score is 0.24dB lower than ours.

To this end, we begin by reviewing various degradation phenomena from Spatial-Wavelet-Fourier perspective and observe that multi-domain transformations can effectively separate degradation representations, providing valuable insights for restoration network design. In the following, we elaborate on the underlying discoveries behind multi-domain perspective.

**(1) Compact Fourier Domain Degradation Representation:** In Fig.1(c), the first row shows the residuals of clear and degraded images, alongside their Fourier-domain representations via Fast Fourier Transform (FFT). Degradation in the spatial domain is often globally diffuse, whereas in the Fourier domain, it is more compact and localized. Specifically, in tasks like deraining and deblurring, degradation primarily affects high frequencies, while in dehazing and low-light enhancement, it concentrates in low frequencies. This suggests that modeling degradation in the Fourier domain offers more efficient solutions. **(2) Strong Separation Restoration Priors:** In subsequent rows of Fig.1(c), we apply Wavelet Transform (WT) to decompose the image into four sub-bands: [LL, LH, HL, HH], followed by FFT to map them into the Fourier

Xingyu Jiang, Ning Gao, Xiuhui Zhang, Hongkun Dou, Hongjue Li and Yue Deng are with Beihang University, Beijing 100191, China; Shaowen Fu is with the Beijing Aerospace Automatic Control Institute; Xiaoqing Zhong is with the China Academy of Space Technology. (e-mail: ydeng@buaa.edu.cn)

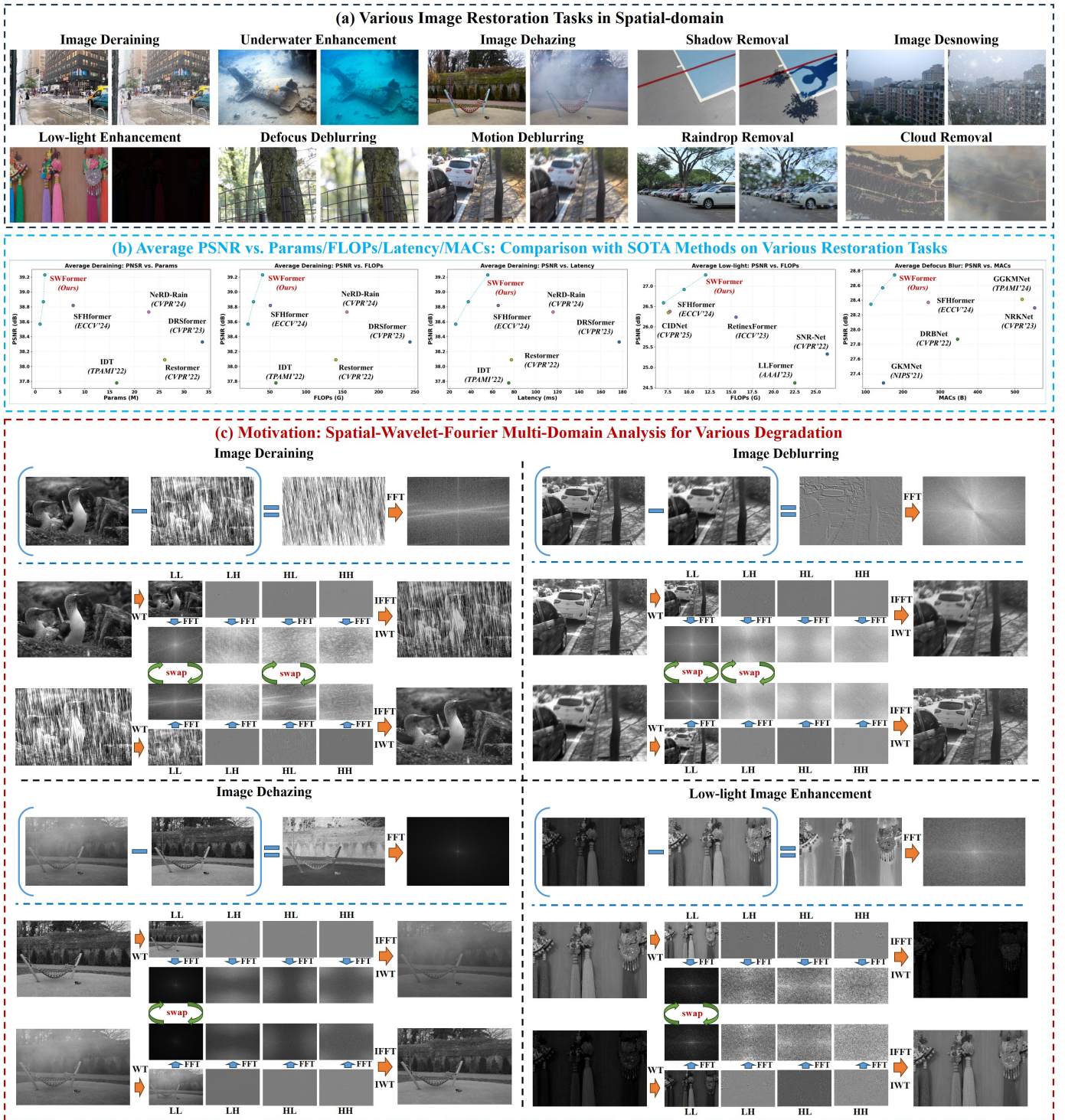


Fig. 1: (a) Spatial-domain representations for various restoration tasks. (b) Performance and model complexity balance: Average PSNR vs. Params/FLOPs/Latency/MACs. We average performance across different benchmarks for statistical characteristics. (c) Motivation: Spatial-Wavelet-Fourier analysis for various degradations. For simplicity, we present the results in grayscale.

domain. We find that degradation tends to concentrate in specific sub-bands, such as LL and HL for deraining, LL and LH for deblurring and LL for dehazing and low-light. We swap the specific sub-bands between the clear and degraded images, and through inverse transformations, recover the corresponding swapped versions. Consequently, the initial clear image transform into its degraded counterpart and conversely,

the degraded image exhibits clear one. This demonstrates that WT and FFT allow us to isolate degradation representations into specific wavelet sub-bands at targeted Fourier frequencies, providing a strong restoration prior for network design. **(3) Efficient Local-Region-Global Receptive Field Modeling:** The Spatial-Wavelet-Fourier multi-domain perspective aligns with local-region-global receptive field modeling, where the spatial

domain captures local features, the wavelet domain models regional features and the Fourier domain encodes global features. Additionally, the Fourier domain's  $O(N \log N)$  computational complexity is more efficient than the  $O(N^2)$  complexity of self-attention. Building on these insights, we integrate these restoration priors into the transformer architecture, enabling efficient image restoration via multi-domain learning.

In this work, we propose SWFormer, a novel restoration backbone designed to tackle various degradation tasks from a multi-domain perspective. Inspired by NAFNet [8], SWFormer introduces key enhancements at both the inter-block and intra-block levels. At the inter-block level, we introduce a Lossless Multi-Input Multi-Output (LMIMO) framework, enabling dynamic output generation at different sizes (small, medium and large) and performance boosting with minimal computational overhead. At the intra-block level, we retain the Transformer architecture but modify the Token Mixer and Feed-Forward Network. Specifically, SWFormer comprises two essential components: the Spatial-Wavelet-Fourier Mixer (SWFM) and the Multi-scale ConvFFN (MSFN). The SWFM replaces self-attention [24] with a Spatial-Wavelet-Fourier tri-branch structure for local-region-global modeling, reducing model complexity. The wavelet branch adopts learnable convolutions to parametrize the wavelet decomposition, while the Fourier branch introduces a gating mechanism to filter frequency components. For the MSFN, we incorporate multi-scale learning to aggregate features from the spatial, wavelet and Fourier domains across different resolutions, enabling more comprehensive and efficient feature fusion.

We evaluate the effectiveness of SWFormer through extensive experiments on 26 widely adopted benchmarks across 10 restoration tasks, including dehazing [58], desnowing [10], rain streak/raindrop removal [71], [90], cloud removal [84], motion blur [66], defocus blur [2], shadow removal [21], underwater enhancement [70] and low-light enhancement [93]. The results demonstrate that SWFormer achieves state-of-the-art (SOTA) performance on most datasets, while maintaining an excellent balance between restoration performance, parameter size, computational cost and inference latency.

We summarize the main contributions as follows:

- We revisit various degradation phenomena from a Spatial-Wavelet-Fourier perspective, providing valuable restoration priors and insights for future network designs.
- We propose SWFormer, a novel and efficient image restoration backbone that handles a wide range of restoration tasks, with a carefully designed architecture at both inter-block and intra-block levels.
- At inter-block level, we introduce a Lossless Multi-Input Multi-Output framework to enhance performance and enable dynamic outputs. At intra-block level, we integrate multi-domain learning into the Transformer for local-region-global modeling and incorporate multi-scale learning for feature aggregation.
- We demonstrate that SWFormer surpasses SOTA methods, maintaining favorable balance between restoration performance, parameter size, computational cost and inference latency across 10 restoration tasks.

Compared to its conference version [43], this present work expands on more detailed discussion, analysis and materials, including new ideas, network architecture designs, additional experimental results and more comprehensive ablation studies. **(1) New Discoveries:** We revisit the restoration priors for various degradation tasks from a Spatial-Wavelet-Fourier multi-domain perspective. Unlike the conference version, we introduce the wavelet domain for more precise separation of degradation across sub-bands, providing valuable insights for network architecture design. **(2) New Architecture Designs:** We introduce new network structures at both the inter-block and intra-block levels compared with the conference version. At the inter-block level, we update the original single-input single-output architecture into a lossless multi-input multi-output framework, enabling dynamic generation of models at varying sizes (small, medium and large) and showcasing the scaling capability of our model. Besides, such framework can improve restoration quality with minimal computational overhead. At the intra-block level, we add a wavelet branch in Token Mixer to extract region features and incorporate gating mechanism in the Fourier branch to replace the dynamic convolution, improving Fourier domain filtering efficiency. **(3) Additional Experiments:** Compared with the conference version, we further validate the effectiveness of SWFormer on two new restoration tasks: remote sensing cloud removal and shadow removal. Additionally, for defocus deblurring, we conduct experiments on a new larger-scale dataset LFDof [79]. Extensive ablation studies confirm the effectiveness of the newly introduced components in our model.

## II. RELATED WORK

In this section, we first review the development of image restoration and then summarize the characteristics of current model architectures at both the inter-block and intra-block levels, highlighting the differences in our method.

### A. Image Restoration

Image restoration is a long-standing ill-posed optimization problem that has drawn significant interest in the computer vision community. To handle this ill-posed nature, additional prior information or statistical constraints are often introduced. Current image restoration methods can be broadly classified into two categories: prior-based methods [36], [46], [100] and data-driven methods [18], [23], [35], [42], [92], [103]. Prior-based methods typically start from the restoration tasks themselves, constructing degradation equations and introducing novel physical assumptions or statistical findings to constrain the solution space, thus solving the ill-posed optimization problem. For example, [36] proposed the dark channel prior for dehazing, [100] introduced the residual channel prior for deraining and [46] proposed the Retinex prior model for low-light. These prior-based methods demonstrate nice statistical properties in certain scenarios, but may fail when the assumptions no longer hold in complex real-world scenes.

Recently, data-driven methods, particularly CNNs [72], [104], have been proposed to overcome the limitations of prior-based approaches. Thanks to novel architectural designs

(such as residual networks [37], feature pyramids [55] and dense blocks [39]) and unique mechanisms (such as attention [72], adversarial learning [25] and multi-kernel [85]), these CNN-based methods have achieved impressive performance in end-to-end manner. More recently, vision transformers [24] have introduced the self-attention mechanism into computer vision, gradually gaining popularity in the low-level vision community. Unlike CNNs, the self-attention captures long-range dependencies through global modeling. Various transformer-based algorithms [92], [103] have demonstrated the significance of global modeling in image restoration and have achieved remarkable success in tasks such as dehazing [83], deraining [12], motion deblurring [45] and low-light enhancement [6]. However, the substantial model complexity introduced by the self-attention poses significant challenges for both training and real-time deployment. As a result, numerous simplification methods [33], [54], [103] for self-attention have been proposed. For instance, Swin-Transformer [63] introduced window self-attention, Restormer [103] proposed channel self-attention and Mambair [33] introduced visual state-space model as an efficient alternative to self-attention. Although these methods have been successful in reducing model complexity, they often come at the cost of decreased performance, making it difficult to strike an optimal balance between performance, model size and computational cost.

Unlike previous studies, we aim to combine the strengths of both prior-based and data-driven methods. By incorporating restoration priors into the design of data-driven model architectures, we propose a customized backbone specifically tailored for image restoration. Specifically, we first revisit the common priors across different degradation processes from spatial-wavelet-Fourier perspective and then leverage multi-

domain learning to achieve local-region-global multi-receptive field modeling, enabling efficient image restoration.

### B. Architecture Design at Inter-block Level

Fig.2 illustrates different designs of inter-block level architecture. Initially, most models [31], [43] adopt a single-input single-output (SISO) architecture in Fig.2(a), where the degraded image is input into the network at the beginning and a clear output is obtained at the end. Recently, multi-input multi-output (MIMO) architectures [19], [20] in Fig.2(b), have gradually become mainstream in model design, in which multi-scale degraded images are input at different stages, with outputs at corresponding stages as well. Compared to SISO, MIMO enhances the extraction of multi-scale features and can be viewed as auxiliary learning. MIMO provides extra constraints to optimize the network at different stages.

In our work, as shown in Fig.2(c), we further introduce the Lossless Multi-Input Multi-Output (LMIMO) architecture based on MIMO. Compared with MIMO, the LMIMO architecture features the following core improvements: (1) For the multi-input part, we employ Wavelet Transform or Pixel Unshuffle [38] for downsampling, which preserves lossless information and enriches the multi-scale feature inputs. (2) For the multi-output part, we utilize Inverse Wavelet Transform or Pixel Shuffle [38] for upsampling, allowing the network to generate restored images at different stages. This design further enables dynamic forward inference within the network. So that, during a single training, we can obtain model variants for small, medium and large sizes, without additional separate training. Ablation experiments show that, compared to SISO and MIMO, LMIMO achieves a significant improvement in restoration performance with minimal computational overhead.

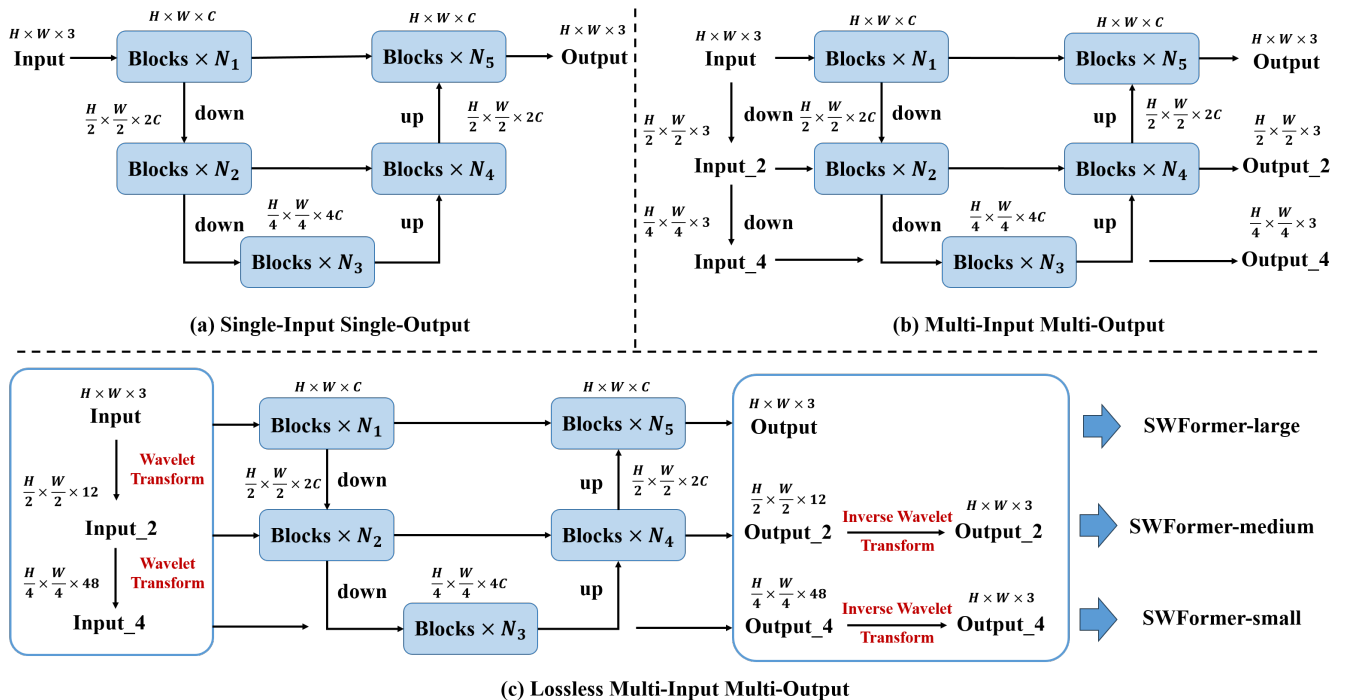


Fig. 2: Inter-block designs: (a) Single-Input Single-Output, (b) Multi-Input Multi-Output, (c) Lossless Multi-Input Multi-Output.

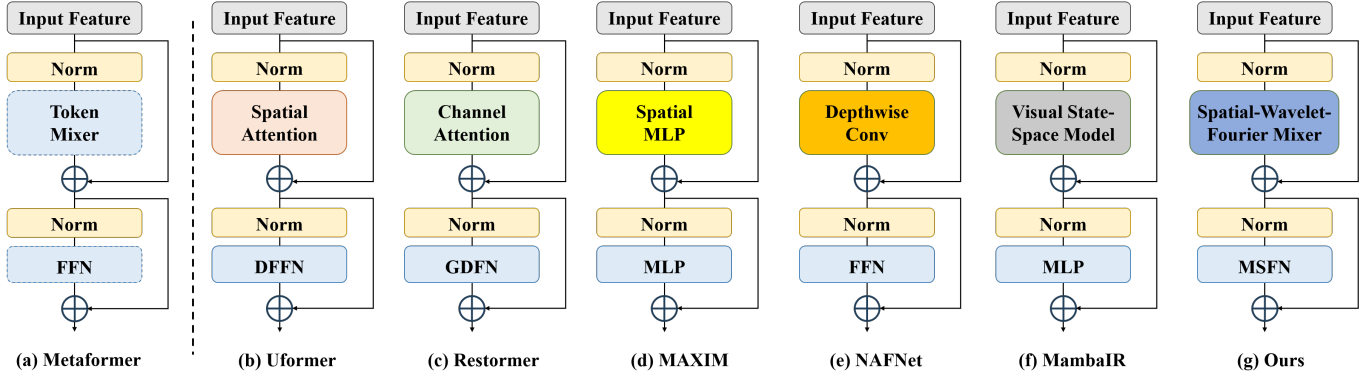


Fig. 3: Comparison of Token Mixer and FFN modules across various restoration methods at Intra-block level.

### C. Architecture Design at Intra-block Level

Fig.3 illustrates the representative intra-block level architecture design based on Transformer. In general, most current image restoration methods adopt metaformer [101] architecture, as shown in Fig.3(a), which retains the overall structure of the Transformer while primarily modifying the Token Mixer and Feed Forward Network (FFN). As shown in Fig.3, Uformer [92] introduces window spatial attention in the Token Mixer to reduce the high complexity of self-attention, meanwhile incorporating convolution in the FFN to provide spatial consistency. Restormer [103] innovatively incorporates channel self-attention in the Token Mixer to simplify computations and introduces gating mechanism in FFN. Methods like MAXIM [87], NAFNet [8] and MambaIR [33] completely discard self-attention, instead utilizing spatial MLP, depthwise convolutions and visual state-space model respectively, to achieve efficient degradation modeling.

In contrast to above approaches, we introduce multi-domain learning in Token Mixer, enabling local-region-global multi-receptive field modeling through Spatial-Wavelet-Fourier feature extraction. In FFN, we incorporate multi-scale learning to fuse Spatial-Wavelet-Fourier features at different resolutions. These fine-grained design choices allow our model to effectively balance restoration performance and model complexity, offering an efficient solution for image restoration.

## III. METHODS

In this section, we first present the overall framework of our SWFormer model. We then describe the core components of the proposed SWFormer block. Finally, we provide the details of the loss functions adopted for SWFormer.

### A. Overall Architecture

Building upon the previously discovered Spatial-Wavelet-Fourier priors and the inter/intra-block level architecture design, we propose the SWFormer framework, as illustrated in Fig.4. Under the LMIMO framework, SWFormer employs a hierarchical encoder-decoder structure consisting of five stages: a two-scale encoder (stage-1 and stage-2), a bottleneck (stage-3) and a two-scale decoder (stage-4 and stage-5). Given a degraded image  $I \in \mathbb{R}^{H \times W \times 3}$ , SWFormer first generates

multi-scale images  $\{I^i, i = 1, 2, 3\} \in \{\mathbb{R}^{\frac{H}{n} \times \frac{W}{n} \times 3 \times 2^{n-1}}, n = 1, 2, 3\}$  through Wavelet Transform, where  $H \times W$  represents the spatial dimensions and  $C$  is the number of channels. Then,  $\{I^i, i = 1, 2, 3\}$  are passed through the Encoder Layer to generate input features at different scales  $\{F_a^i, i = 1, 2, 3\} \in \{\mathbb{R}^{\frac{H}{n} \times \frac{W}{n} \times nC}, n = 1, 2, 3\}$ , where the Encoder Layer consists of multiple  $3 \times 3$  convolutions for dimensional expansion. Subsequently,  $\{F_a^i, i = 1, 2, 3\}$  are passed through the five-stage hierarchical encoder-decoder structure. Between each stage, the spatial resolution is progressively reduced using Pixel Unshuffle downsampling in the two-scale encoder and then increased using Pixel Shuffle upsampling in the two-scale decoder. Within each stage, multi-scale input features  $\{F_a^i, i = 1, 2, 3\}$  are processed through  $\{N^i, i = 1, 2, 3\}$  SWFormer blocks to extract multi-scale output features  $\{F_z^i, i = 1, \dots, 5\} \in \{\mathbb{R}^{\frac{H}{n} \times \frac{W}{n} \times nC}, n = 1, 2, 3\}$ . To preserve structural and textural details for restoration, low-level latent features  $\{F_z^i, i = 1, 2\}$  are concatenated with high-level latent features  $\{F_z^i, i = 4, 3\}$  through skip connections. Finally, the Decoder Layer maps  $\{F_z^i, i = 3, 4, 5\}$  to the residual degraded image  $\{R^i, i = 1, 2, 3\} \in \{\mathbb{R}^{\frac{H}{n} \times \frac{W}{n} \times 3 \times 2^{n-1}}, n = 1, 2, 3\}$ , which is used to obtain multi-scale clear images  $\{O^i, i = 1, 2, 3\}$  via  $\{O^i = I^i + R^i, i = 1, 2, 3\}$ , where the Decoder Layer consists of multiple  $3 \times 3$  convolutions for dimensional reduction. In the following two subsections, we will detail the configurations of the two core modules: SWFM and MSFN.

### B. Spatial-Wavelet-Fourier Mixer

As reflected by the its name, SWFM is designed to implement a local-region-global modeling structure, consisting of three key branches: the spatial-domain branch for local perception, the wavelet-domain branch for region perception and the Fourier-domain branch for global perception. As shown in Fig.4, SWFM first applies a point-wise (PW) convolution  $\tilde{f}_{pw}$  to expand the channel dimension of the input feature  $F_0 \in \mathbb{R}^{H \times W \times C}$ . Then, the expanded feature  $F_1 \in \mathbb{R}^{H \times W \times 4C}$  is split into three parts:  $F_{sp} \in \mathbb{R}^{H \times W \times C}$ ,  $F_{wa} \in \mathbb{R}^{H \times W \times C}$  and  $F_{fr} \in \mathbb{R}^{H \times W \times 2C}$ , which are then processed through the spatial-domain branch, wavelet-domain branch and Fourier-domain branch, respectively. Next, we apply a channel-attention operation (see Fig.4(d)) to maintain feature fusion at the channel level. Finally, another point-

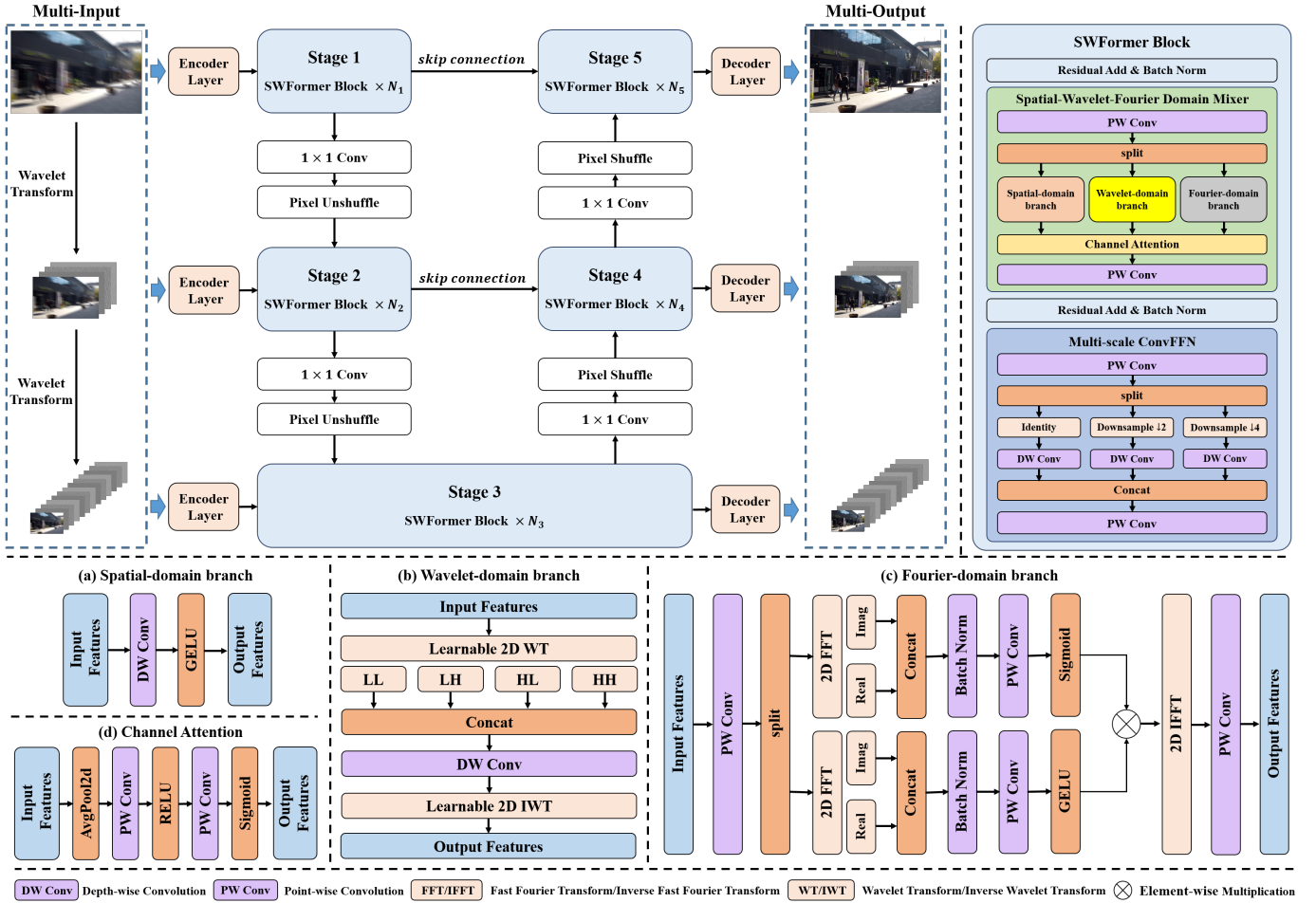


Fig. 4: The overall framework of our proposed SWFormer and its detailed components.

wise convolution is applied to obtain the reduced feature  $F_2 \in \mathbb{R}^{H \times W \times C}$ . The detailed implementation of the spatial-domain branch, wavelet-domain branch and Fourier-domain branch is described as follows.

1) *Spatial-domain Branch*: The spatial-domain branch focuses on extracting spatial features for local modeling at the pixel level. Given the inherent local perception property of convolutions, we use depth-wise convolution to extract local spatial features. Specifically, as shown in Fig.4(a), the input feature  $F_{sp}$  in the spatial-domain branch is passed sequentially through a depth-wise convolution  $\tilde{f}_{dw}$  (DW) followed by a GELU activation function  $\sigma$  to obtain the deep spatial feature  $F_{sp}^d \in \mathbb{R}^{H \times W \times C}$ . The process can be expressed as:

$$F_{sp}^d = \sigma \cdot \tilde{f}_{dw}(F_{sp}) \quad (1)$$

2) *Wavelet-domain Branch*: The wavelet-domain branch focuses on extracting wavelet features for region-level modeling across different wavelet components. Here, we briefly revisit the wavelet transform (WT), which is widely used for analyzing the multi-scale and multi-directional characteristics of images. Given a 2D image  $x \in \mathbb{R}^{H \times W \times 3}$ , the wavelet transform  $\mathcal{W}$  (WT) decomposes it into four components  $[LL, LH, HL, HH]$ , which can be formulated as:

$$\mathcal{W}(x) = \begin{cases} LL = ((x * h) * h^\top) \downarrow_{2,2}, \\ LH = ((x * h) * g^\top) \downarrow_{2,2}, \\ HL = ((x * g) * h^\top) \downarrow_{2,2}, \\ HH = ((x * g) * g^\top) \downarrow_{2,2} \end{cases} \quad (2)$$

where  $h$  and  $g$  are low-pass and high-pass filters,  $*$  denotes convolution and  $\downarrow_{2,2}$  represents 2D downsampling. As shown in Eq.2, the four components  $[LL, LH, HL, HH]$  correspond to the low-frequency approximation and high-frequency details (horizontal, vertical, and diagonal) of the image, enabling effective region-level feature extraction via downsampling. The structure of the wavelet-domain branch is detailed in Fig.4(b). Specifically, the input feature  $F_{wa}$  is passed through a learnable 2D wavelet transform  $\mathcal{W}_\phi$  to obtain the four wavelet components  $\{F_{LL}, F_{LH}, F_{HL}, F_{HH}\} \in \mathbb{R}^{\frac{H}{2} \times \frac{W}{2} \times C}$ , where  $\phi$  represents parameterized convolutions. These components are concatenated along the channel dimension and processed through a depth-wise convolution  $\tilde{f}_{dw}$  for feature extraction in the wavelet domain. Finally, a learnable 2D inverse wavelet transform (IWT) reconstructs the modulated deep wavelet feature  $F_{wa}^d \in \mathbb{R}^{H \times W \times C}$ . This process can be formulated as:

$$F_{wa}^d = \mathcal{W}^{-1} \left( \sigma \cdot \tilde{f}_{dw} (\text{Concat}[F_{LL}, F_{LH}, F_{HL}, F_{HH}]) \right) \quad (3)$$

3) *Fourier-domain Branch*: The frequency-domain branch focuses on capturing frequency features for global modeling around the entire image. Here, we review the Fourier transform, which is widely used for analyzing the frequency characteristic of images. Given an image  $x$ , the fast Fourier transform  $\mathcal{F}$  converts it to frequency space as the complex component  $\mathcal{F}(x)$ , which is expressed as:

$$\mathcal{F}(x)(u, v) = \frac{1}{\sqrt{HW}} \sum_{h=0}^{H-1} \sum_{w=0}^{W-1} x(h, w) e^{-j2\pi(\frac{h}{H}u + \frac{w}{W}v)} \quad (4)$$

where  $u$  and  $v$  are the coordinates of the Fourier space.  $\mathcal{F}^{-1}$  represents the inverse fast Fourier transform (IFFT). As shown in Eq.4, individual components in the frequency domain correspond to entire pixel sets in the spatial domain. Unlike the frequency dynamic convolutions in the conference version, which improve restoration performance but slow down inference speed, we adopt a gating mechanism to filter the frequency components directly. As illustrated in Fig.4(c), the input feature  $F_{fr}$  is passed through a PW convolution and split into two gating vectors:  $F_{fr}^1 \in \mathbb{R}^{H \times W \times C}$  and  $F_{fr}^2 \in \mathbb{R}^{H \times W \times C}$ . We then apply 2D FFT to map the features to the Fourier domain and concatenate the real and imaginary parts, producing joint features  $F_j^1 \in \mathbb{R}^{H \times W \times 2C}$  and  $F_j^2 \in \mathbb{R}^{H \times W \times 2C}$ .  $F_j^1$  undergoes batch normalization, a PW convolution and a GELU activation function to obtain frequency features  $F_{fd} \in \mathbb{R}^{H \times W \times 2C}$ , while  $F_j^2$  is processed with batch normalization, a PW convolution and a Sigmoid activation to produce gating features  $F_{ga} \in \mathbb{R}^{H \times W \times 2C}$ . Finally, the two features are element-wise multiplied, mapped back to the spatial domain via 2D IFFT, and reduced using a PW convolution  $\tilde{f}_{pw}$  to obtain the modulated deep Fourier feature  $F_{fr}^d \in \mathbb{R}^{H \times W \times C}$ . This process can be formulated as:

$$F_{fr}^d = \tilde{f}_{pw} (\mathcal{F}^{-1} (F_j^1 \odot F_j^2)) \quad (5)$$

### C. Multi-Scale ConvFFN

The Feed-Forward Network is a crucial module in Transformers, and in this work, we use it to integrate the local-region-global features extracted by the token mixer. Specifically, we introduce multi-scale learning to fuse features across different resolutions. As shown in Fig.4, MSFN starts by applying a PW convolution to double the dimension of the input features  $F_2$ . The expanded features  $F_3 \in \mathbb{R}^{H \times W \times 2C}$  are split into three parts: one part undergoes identity operation, another is downsampled by a factor of two, and the third is downsampled by a factor of four. These components are processed through DW convolutions to capture local connections. After aggregating the multi-scale features, a final PW convolution reduces the dimension. This design efficiently fuses features from multiple scales, capturing rich spatial information while maintaining computational efficiency.

### D. Loss Function

To align with the model design, we introduce a multi-domain loss in the optimization flow, as shown in Eq.6. This

loss consists of three components: spatial-domain, wavelet-domain and Fourier-domain losses.

$$L^i = \|O^i - G^i\|_1 + \|\mathcal{W}(O^i) - \mathcal{W}(G^i)\|_1 + \lambda \|\mathcal{F}(O^i) - \mathcal{F}(G^i)\|_1, \quad i = 1, 2, 3 \quad (6)$$

Here, the L1 loss regularizes  $\{O^i, i = 1, 2, 3\}$  to match multi-scale ground truth  $\{G^i, i = 1, 2, 3\}$ . The hyperparameter  $\lambda$  is set to 0.1 to balance the contributions of each domain loss.

## IV. EXPERIMENTAL RESULTS

To evaluate our SWFormer effectiveness, we conduct extensive experiments on common image restoration tasks. In tables, the best and second-best quality scores of the evaluated methods are **highlighted** and underlined.

### A. Experimental Settings

1) *Datasets*: We adopt RESIDE [50], O-HAZE [5], NH-HAZE [4] and DENSE-HAZE [3] for dehazing; Rain200H [97], Rain200L [97], DDN-Data [27], DID-Data [106] and SPA-Data [90] for deraining; Raindrop [71] for raindrop removal; CSD [11], SRRS [10] and Snow100K [62] for desnowing; UIEB [51] and LSUI [70] for underwater enhancement; LOL-v1 [93] and LOL-v2 [98] for low-light enhancement; GoPro [66] and HIDE [81] for motion deblurring; DPDD [2] and LFDof [79] for defocus deblurring; AISTD [47] for shadow removal; CUHK-CR [84] for cloud removal. More details of dataset scales and resolutions can be found in Supplementary material.

2) *Implementation Details*: AdamW optimizer [65] with  $\beta_1$  and  $\beta_2$  equal to 0.9 and 0.999 is used to train SWFormer. The initial learning rate is set as  $10^{-3}$ . We adopt the cosine annealing strategy [64] to train the models, where the learning rate gradually decreases from the initial learning rate to  $10^{-6}$ . All experiments are implemented by PyTorch [69] 1.7.1 with four NVIDIA 3090 GPUs. More implementation details for each restoration tasks can be found in Supplementary material.

### B. Results on Rain Streak/Raindrop Removal Task

We conduct rain streak/raindrop removal experiments on six widely used public datasets, including four synthetic datasets, Rain200L [97], Rain200H [97], DID-Data [106] and DDN-Data [27], and two real-world datasets, SPA-Data [90] and Raindrop [71]. Tab.II presents the quantitative comparison results for rain streak removal. Compared to the latest SOTA

TABLE I: Quantitative evaluations on raindrop removal.

Methods	Raindrop-A [71]		Raindrop-B [71]	
	PSNR $\uparrow$	SSIM $\uparrow$	PSNR $\uparrow$	SSIM $\uparrow$
(CVPR'19)DuRN [59]	31.24	0.926	25.32	0.817
(CVPR'18)AttentiveGAN [71]	31.59	0.917	25.05	0.811
(TPAMI'22)IDT [94]	31.87	0.931	-	-
(CVPR'22)MAXIM [87]	31.87	0.935	25.74	0.827
(TPAMI'23)RainDropDiff128 [68]	32.43	0.933	-	-
(ICCV'23)UDR-S <sup>2</sup> Former [9]	32.64	0.943	26.92	0.832
(CVPR'24)AST [111]	32.45	0.937	24.99	0.806
(ECCV'24)SFHformer [43]	33.10	0.946	27.17	<b>0.838</b>
(Ours)SWFormer-s	33.29	0.945	27.34	0.834
(Ours)SWFormer-m	<b>33.50</b>	<b>0.946</b>	27.44	0.835
(Ours)SWFormer-l	<b>33.55</b>	<b>0.948</b>	<b>27.48</b>	<u>0.835</u>

TABLE II: Quantitative evaluations on synthetic and real-world deraining datasets.

Method	Synthetic								Real	
	Rain200L [97]		Rain200H [97]		DDN-Data [27]		DID-Data [106]		SPA-Data [90]	
	PSNR $\uparrow$	SSIM $\uparrow$								
(CVPR'21)MPRNet [104]	39.47	0.9825	30.67	0.9110	33.10	0.9347	33.99	0.9590	43.64	0.9844
(AAAI'21)DualGCN [28]	40.73	0.9886	31.15	0.9125	33.01	0.9489	34.37	0.9620	44.18	0.9902
(ICCV'21)SPDNet [100]	40.50	0.9875	31.28	0.9207	33.15	0.9457	34.57	0.9560	43.20	0.9871
(CVPR'22)Uformer [92]	40.20	0.9860	30.80	0.9105	33.95	0.9545	35.02	0.9621	46.13	0.9913
(CVPR'22)Restormer [103]	40.99	0.9890	32.00	0.9329	34.20	0.9571	35.29	0.9641	47.98	0.9921
(TPAMI'22)IDT [94]	40.74	0.9884	32.10	0.9344	33.84	0.9549	34.89	0.9623	47.35	0.9930
(AAAI'23)HCT-FFN [14]	39.70	0.9850	31.51	0.9100	33.00	0.9502	33.96	0.9592	45.79	0.9898
(CVPR'23)DRSformer [12]	41.23	0.9894	32.17	0.9326	34.35	0.9588	35.35	0.9646	48.54	0.9924
(CVPR'24)NeRD-Rain [13]	41.71	0.9903	32.40	0.9373	<u>34.45</u>	0.9596	<u>35.53</u>	<u>0.9659</u>	49.58	0.9940
(ECCV'24)FADformer [31]	41.80	0.9906	32.48	0.9359	34.42	<u>0.9602</u>	35.48	0.9657	49.21	0.9934
(ECCV'24)SFHformer [43]	41.85	0.9908	32.33	0.9351	34.38	0.9594	35.44	0.9655	<u>50.11</u>	<u>0.9942</u>
(Ours)SWFormer-s	42.01	0.9908	32.43	0.9345	34.18	0.9573	35.18	0.9639	49.03	0.9936
(Ours)SWFormer-m	<u>42.23</u>	<u>0.9913</u>	<u>32.69</u>	<u>0.9377</u>	34.36	0.9592	35.42	0.9654	49.66	0.9941
<b>(Ours)SWFormer-l</b>	<b>42.70</b>	<b>0.9922</b>	<b>33.09</b>	<b>0.9441</b>	<b>34.51</b>	<b>0.9608</b>	<b>35.58</b>	<b>0.9664</b>	<b>50.28</b>	<b>0.9943</b>

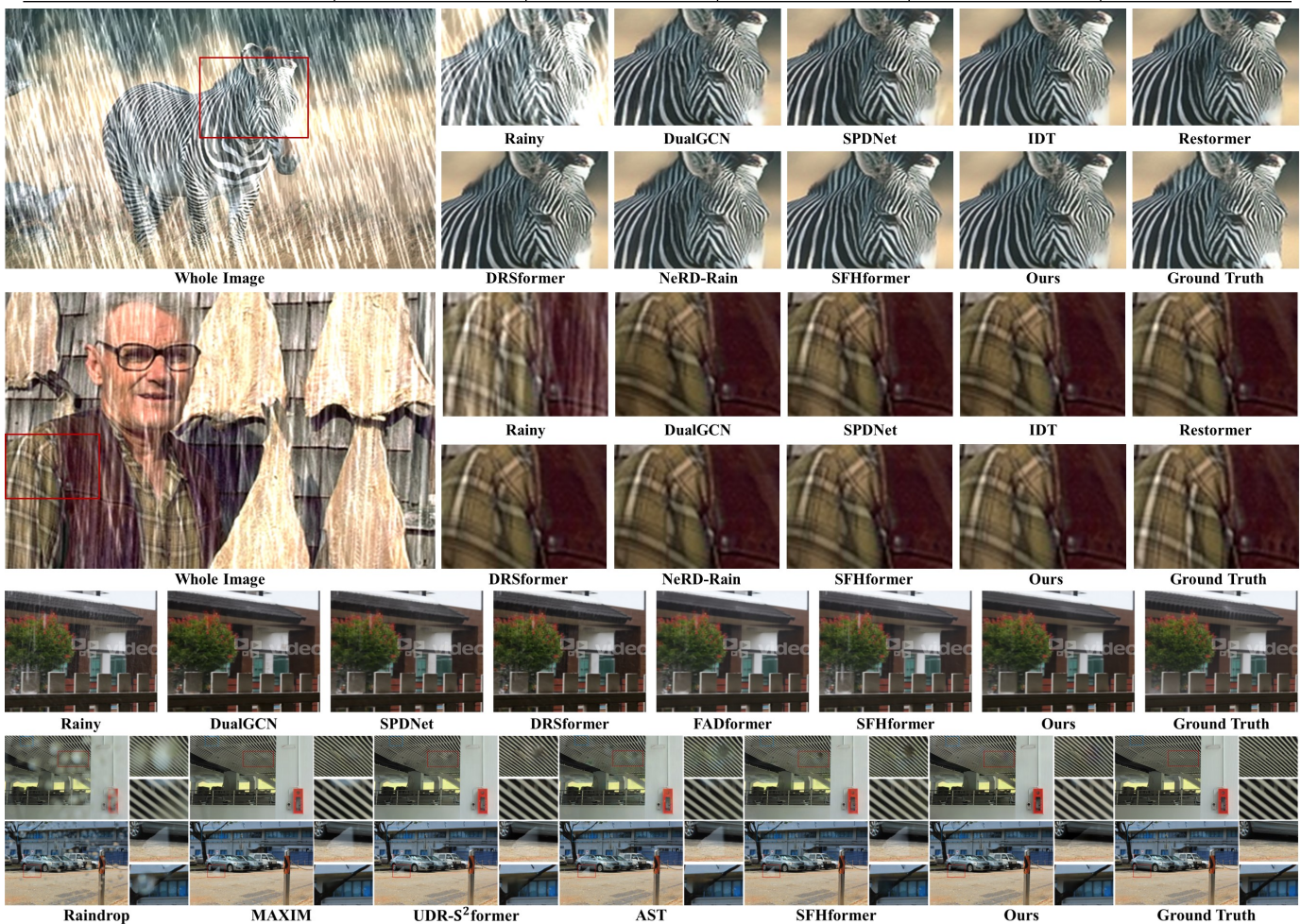


Fig. 5: The quantitative evaluation results on synthetic/real-world rain streak removal and raindrop removal.

methods, our proposed SWFormer achieves the best performance in terms of PSNR and SSIM across all datasets. Notably, on the Rain200L and Rain200H datasets, even our smallest model, SWFormer-small, outperforms SFHFormer [43] in PSNR. Tab.I also presents the quantitative results for raindrop removal, where SWFormer demonstrates a highly competitive performance advantage. Fig.5 shows the quali-

tative comparison results for synthetic rain streak removal, real-world rain streak removal and raindrop removal, presented from top to bottom. Our method consistently delivers superior rain removal results, excelling in texture detail preservation and raindrop repair. In contrast, other methods either fail to effectively remove rain or over-remove it, mistakenly eliminating white stripes or clothing bands as rain streaks.

TABLE III: Quantitative evaluations on synthetic and real-world low-light enhancement.

Method	LOL-v1 [93]				LOL-v2-real [98]				LOL-v2-syn [98]			
	Normal		GT Mean		Normal		GT Mean		Normal		GT Mean	
	PSNR↑	SSIM↑	PSNR↑	SSIM↑	PSNR↑	SSIM↑	PSNR↑	SSIM↑	PSNR↑	SSIM↑	PSNR↑	SSIM↑
(TPAMI'20)3DLUT [105]	14.35	0.445	21.35	0.585	17.59	0.721	20.19	0.745	18.04	0.800	22.17	0.854
(TIP'21)Sparse [98]	17.20	0.640	-	-	20.06	0.816	-	-	22.05	0.905	-	-
(CVPR'21)RUAS [57]	16.41	0.500	18.65	0.518	15.33	0.488	19.06	0.510	13.77	0.638	16.58	0.719
(AAAI'22)LLFlow [91]	21.15	0.854	24.99	0.871	17.43	0.831	25.42	0.877	24.81	0.919	27.96	0.930
(CVPR'22)Restormer [103]	22.37	0.816	26.68	0.853	18.69	0.834	26.12	0.853	21.41	0.830	25.43	0.859
(ECCV'22)LEDNet [110]	20.63	0.823	25.47	0.846	19.94	0.827	27.81	0.870	23.71	0.914	27.37	0.928
(CVPR'22)SNR-Net [95]	24.61	0.842	26.72	0.851	21.48	0.849	27.21	0.871	24.14	0.928	27.79	0.941
(CVPR'23)PairLIE [30]	19.51	0.736	23.53	0.755	19.89	0.778	24.03	0.803	-	-	-	-
(AAAI'23)LLFormer [89]	23.65	0.816	25.76	0.823	20.06	0.792	26.20	0.819	24.04	0.909	28.01	0.927
(ICCV'23)RetinexFormer [6]	25.15	0.846	27.14	0.850	22.79	0.840	27.69	0.856	25.67	0.930	28.99	0.939
(ECCV'24)SFHFormer [43]	24.29	0.862	26.97	0.869	<u>23.78</u>	<u>0.872</u>	<u>28.36</u>	<u>0.883</u>	25.80	0.937	29.06	0.940
(CVPR'25)CIDNet [96]	23.50	<u>0.870</u>	<b>28.14</b>	<u>0.889</u>	23.43	0.862	27.76	0.881	25.71	<u>0.942</u>	29.57	<u>0.950</u>
(Ours)SWFormer-s	25.26	0.861	27.52	0.864	22.79	0.854	28.51	0.879	26.17	0.932	29.31	0.941
(Ours)SWFormer-m	<u>25.65</u>	<u>0.870</u>	<u>27.96</u>	0.882	23.42	0.854	28.32	0.876	<u>26.55</u>	0.934	<u>29.63</u>	0.944
(Ours)SWFormer-l	<b>25.70</b>	<b>0.876</b>	<b>28.14</b>	<b>0.892</b>	<b>23.86</b>	<b>0.877</b>	<b>28.72</b>	<b>0.896</b>	<b>27.01</b>	<b>0.943</b>	<b>30.26</b>	<b>0.952</b>

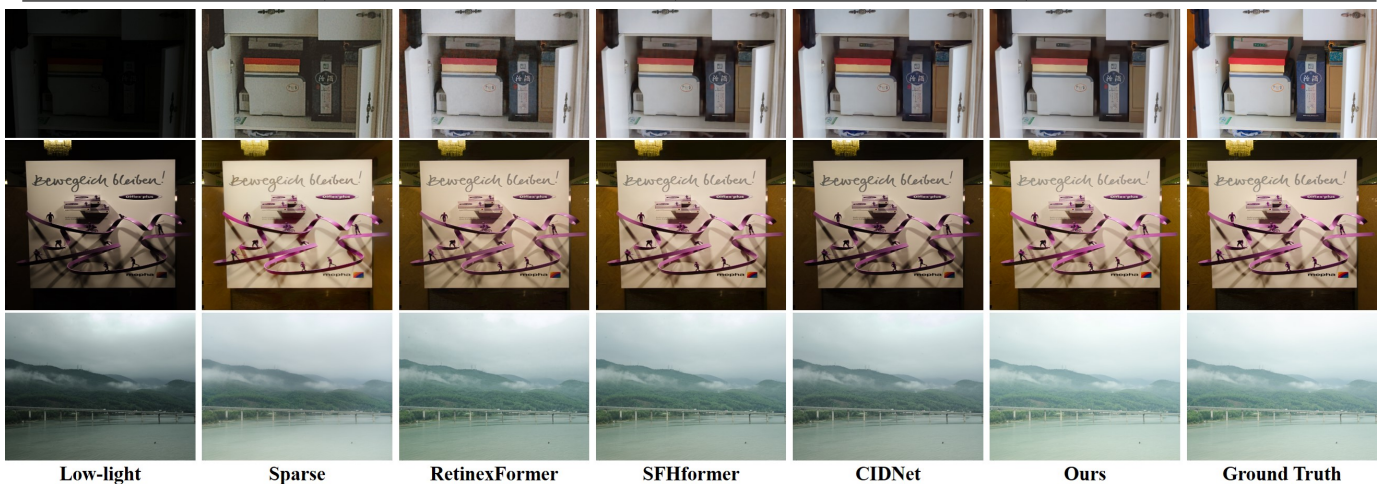


Fig. 6: The quantitative evaluation results on synthetic and real-world low-light enhancement.

C. Results on Low-light Image Enhancement Task

We conduct low-light image enhancement experiments on three widely recognized public datasets: LOLv1 [93], LOLv2-real [98] (real-world low-light dataset) and LOLv2-syn [98] (synthetic low-light dataset). Tab.III presents the quantitative comparison results across these datasets. To provide a comprehensive evaluation of our approach, we compute PSNR and SSIM using two commonly employed methods: the standard computation and a variant with GT Mean preprocessing [96]. Compared to the most recent state-of-the-art methods, our proposed SWFormer consistently achieves superior performance on all three datasets, using both calculation methods. Specifically, our model outperforms SFHFormer [43], demonstrating PSNR improvements of 1.41 dB and 1.21 dB on the LOLv1 and LOLv2-syn datasets, respectively. Fig.6 displays the qualitative comparison results for low-light enhancement. Our method excels in light correction and noise removal, producing the most visually appealing and realistic results. In contrast, RetinexFormer [6] struggles with noise removal, failing to maintain a clean image, while CIDNet [96] demonstrates limitations in light correction, leaving the restored images with unnatural lighting.

D. Results on Image Dehazing Task

We conduct dehazing experiments on five widely established public datasets, including two large-scale synthetic datasets, ITS [50] and OTS [50], as well as three high-resolution real-world outdoor dehazing datasets: O-HAZE [5], NH-HAZE [4] and DENSE-HAZE [3], which cover a range of dehazing scenarios such as outdoor, uneven and heavy haze removal. Tab.IV presents the quantitative comparison results for the dehazing task. Compared to the latest advanced methods, our proposed SWFormer consistently achieves the best restoration performance in terms of both PSNR and SSIM across all datasets. Notably, on the DENSE-HAZE dataset, our model outperforms SFHFormer [43] by a 0.54 dB PSNR improvement, demonstrating its capability in handling extreme weather conditions, particularly heavy haze. Fig.7 illustrates the qualitative comparison results. Our method succeeds in delivering superior dehazing outcomes, whether for real-world outdoor dehazing or challenging uneven dehazing scenarios. A key strength of SWFormer lies in its remarkable performance in color correction. For instance, it effectively restores the natural color tones of red wooden planks and purple streetlights, ensuring more accurate and visually appealing results.

TABLE IV: Quantitative evaluations on the synthetic and real-world dehazing.

Method	ITS [50]		OTS [50]		O-HAZE [5]		NH-HAZE [4]		DENSE-HAZE [3]	
	SOTS-indoor		SOTS-outdoor		PSNR↑	SSIM↑	PSNR↑	SSIM↑	PSNR↑	SSIM↑
	PSNR↑	SSIM↑	PSNR↑	SSIM↑						
(ICCV'17)AOD-Net [49]	20.51	0.8164	24.14	0.9203	15.03	0.54	15.40	0.57	13.14	0.41
(ICCV'19)GridDehazeNet [58]	32.16	0.9845	30.86	0.9827	22.11	0.71	13.80	0.54	-	-
(CVPR'20)MSBDN [23]	33.67	0.9856	33.48	0.9824	24.36	0.75	19.23	0.71	15.37	0.49
(AAAI'20)FFA-Net [72]	36.39	0.9894	33.57	0.9842	22.12	0.77	19.87	0.69	14.39	0.45
(CVPR'22)DeHamer [32]	36.63	0.9881	35.18	0.9860	24.64	0.77	20.66	0.68	16.62	0.56
(ECCV'22)PMNet [99]	38.41	0.9900	34.74	0.9850	24.64	0.83	20.42	0.73	16.79	0.51
(TIP'23)Dehazeformer [83]	38.46	0.9940	34.29	0.9830	25.13	0.77	19.11	0.66	-	-
(ICCV'23)FocalNet [18]	40.82	0.9960	37.71	<u>0.9950</u>	25.50	<u>0.94</u>	20.43	0.79	17.07	0.63
(CVPR'23)C <sup>2</sup> PNet [109]	42.56	0.9954	36.68	0.9900	-	-	-	-	16.88	0.57
(ICCV'23)MB-TaylorFormer [73]	42.64	0.9940	38.09	0.9910	25.31	0.78	-	-	16.44	0.57
(ECCV'24)SFHformer [43]	43.03	0.9966	38.83	<b>0.9951</b>	<u>25.81</u>	<u>0.94</u>	<u>20.73</u>	<u>0.80</u>	17.84	<b>0.68</b>
(Ours)SWFormer-s	41.86	0.9962	37.62	0.9945	22.90	0.76	19.17	0.70	17.57	<u>0.65</u>
(Ours)SWFormer-m	42.54	0.9965	38.57	0.9950	23.91	0.84	18.44	0.72	<u>18.04</u>	<b>0.68</b>
(Ours)SWFormer-l	<b>43.21</b>	<b>0.9968</b>	<b>39.04</b>	<b>0.9951</b>	<b>25.94</b>	<b>0.95</b>	<b>20.86</b>	<b>0.82</b>	<b>18.38</b>	<b>0.68</b>

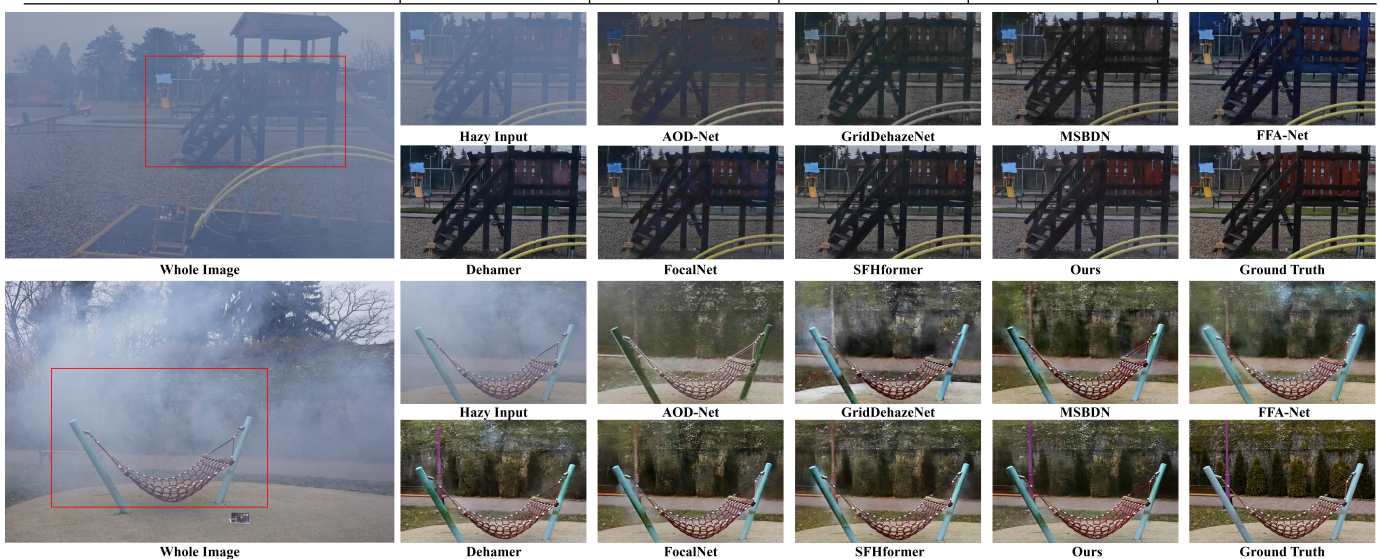


Fig. 7: The quantitative evaluation results on synthetic and real-world image dehazing.

E. Results on Motion Deblurring Task

We perform motion blur removal experiments on two prominent large-scale benchmarks: GoPro [66] and HIDE [81]. To assess the generalization capabilities of our approach, our model is trained exclusively on the GoPro dataset and then applied directly to the HIDE dataset. Tab. V presents the quantitative comparison results for motion blur removal, underscoring the effectiveness of our method. In comparison to the latest state-of-the-art methods, our proposed SWFormer consistently outperforms existing models in restoration performance. Notably, on the HIDE dataset, our model achieves a substantial 0.41 dB PSNR improvement over SFHFormer [43], demonstrating its enhanced generalization ability when applied to previously unseen data. Fig. 8 illustrates the qualitative comparison results for motion blur removal. Our method stands out in its ability to recover fine high-frequency details, particularly in heavily degraded areas such as license plates and text, where precise clarity is paramount. In contrast, other methods introduce noticeable artifacts into their restored images, and in some instances, fail to adequately remove the blur.

TABLE V: Quantitative evaluations on motion deblurring.

Method	GoPro [66]		HIDE [81]	
	PSNR↑	SSIM↑	PSNR↑	SSIM↑
(ICCV'21)MIMO-UNet+ [16]	32.45	0.957	29.99	0.930
(CVPR'21)MPRNet [104]	32.66	0.959	30.96	0.939
(CVPR'22)Restormer [103]	32.92	0.961	31.22	0.942
(ECCV'22)Stripformer [86]	33.08	0.962	31.03	0.940
(ECCV'22)MPRNet-local [17]	33.31	0.964	31.19	0.942
(ECCV'22)Restormer-local [17]	33.57	0.966	31.49	0.945
(ECCV'22)NAFNet [8]	33.71	0.967	31.31	0.943
(ICLR'23)SFNet [20]	33.27	0.963	31.10	0.941
(ICCV'23)icDPMs-SA [77]	33.20	0.963	30.96	0.938
(CVPR'23)GRL [54]	33.93	<u>0.968</u>	31.62	0.947
(ECCV'24)X-Restormer [15]	33.44	0.946	31.76	0.930
(CVPR'24)MISC Filter [56]	<u>34.10</u>	<b>0.969</b>	31.66	0.946
(ECCV'24)SFHformer [43]	34.01	<b>0.969</b>	31.66	0.948
(Ours)SWFormer-s	33.55	0.963	31.27	0.943
(Ours)SWFormer-m	33.94	0.967	31.72	<u>0.948</u>
(Ours)SWFormer-l	<b>34.21</b>	<b>0.969</b>	<b>32.07</b>	<b>0.950</b>

F. Results on Defocus Deblurring Task

Building on the conference version [43], we perform defocus blur removal experiments on two widely used real-world public datasets: DPDD [2] and the newly introduced large-



Fig. 8: The quantitative evaluation results on motion deblurring.



Fig. 9: The quantitative evaluation results on defocus deblurring.

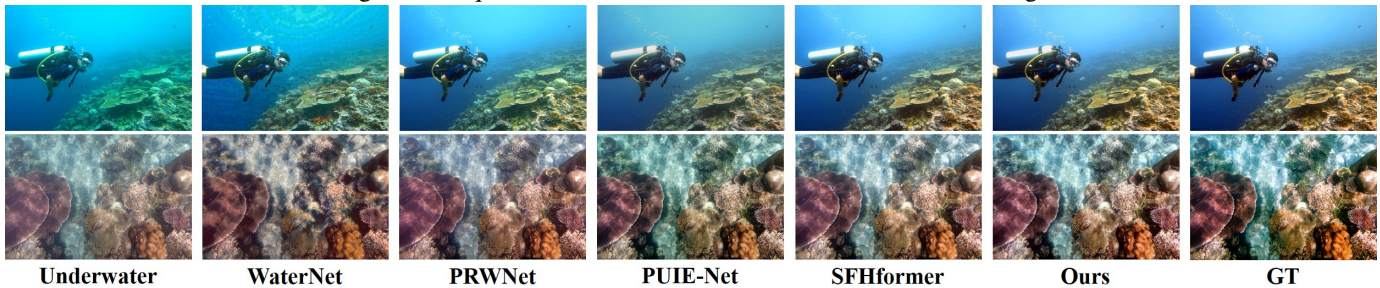


Fig. 10: The quantitative evaluation results on underwater enhancement.

TABLE VI: Quantitative evaluations on defocus blur.

Method	DPDD [2]			LFDof [79]		
	PSNR $\uparrow$	SSIM $\uparrow$	LPIPS $\downarrow$	PSNR $\uparrow$	SSIM $\uparrow$	LPIPS $\downarrow$
(TIP'21)AIFNet [79]	24.213	0.742	0.309	29.677	0.884	0.202
(WACV'22)MDP [1]	25.347	0.763	0.268	28.069	0.834	0.185
(CVPR'21)KPAC [82]	25.221	0.774	0.226	28.942	0.857	0.174
(CVPR'21)IFANet [48]	25.366	0.789	0.217	29.787	0.872	0.154
(NIPS'21)GKMNet [74]	25.468	0.789	0.219	29.081	0.867	0.171
(CVPR'22)DRBNet [80]	25.485	0.792	0.254	30.253	0.883	0.147
(CVPR'23)NRKNet [75]	26.109	0.810	<b>0.210</b>	30.481	0.884	0.147
(ECCV'24)SFHformer [43]	26.118	0.807	0.222	30.623	0.886	0.146
(TPAMI'24)GGKMNet [76]	<b>26.272</b>	0.810	0.215	30.552	0.886	0.154
(Ours)SWFormer-s	26.126	0.810	0.220	30.563	0.884	0.142
(Ours)SWFormer-m	26.184	0.817	0.219	30.954	0.892	0.141
(Ours)SWFormer-l	26.220	<b>0.819</b>	0.221	<b>31.270</b>	<b>0.898</b>	<b>0.133</b>

scale LFDof [79] dataset. Tab.VI presents the quantitative comparison results for defocus blur removal. Our proposed SWFormer demonstrates exceptional performance across all datasets. Notably, on the LFDof dataset, our model achieves the best performance in terms of PSNR, SSIM, and LPIPS. Fig.9 presents the qualitative comparison results. Visually, our method recovers sharper high-frequency details, crucial for accurately restoring fine structures such as text and edges. In contrast, NRKNet [75] suffers from numerical overflow issues, resulting in degraded performance and less precise restoration.

TABLE VII: Evaluations on underwater enhancement.

Method	L-400 [70]			U-90 [51]		
	PSNR $\uparrow$	SSIM $\uparrow$	UCIQE $\uparrow$	PSNR $\uparrow$	SSIM $\uparrow$	UCIQE $\uparrow$
(TIP'20)WaterNet [51]	23.38	0.9152	0.5729	16.31	0.7970	0.5777
(ICCV'21)PRWNet [41]	27.83	0.9268	0.5801	20.79	0.8231	0.5830
(AAAI'21)Shallow-UWNet [67]	20.56	0.7675	0.5517	18.28	0.8553	0.5517
(TIP'23)U-shape Trans [70]	24.16	0.9184	0.5871	21.25	0.8432	0.5882
(ECCV'22)PUIE-Net [29]	21.28	0.8615	0.5887	21.38	0.8821	0.5887
(TGRS'22)URSCT-SESR [78]	29.31	0.9318	0.5890	22.72	0.9108	<b>0.6140</b>
(ECCV'24)SFHformer [43]	30.18	0.9449	<b>0.5943</b>	23.54	0.9177	0.6020
(Ours)SWFormer-s	30.16	0.9422	0.5907	23.10	0.9083	0.5990
(Ours)SWFormer-m	30.49	0.9447	0.5921	23.46	0.9138	0.5975
(Ours)SWFormer-l	<b>30.56</b>	<b>0.9467</b>	0.5932	<b>23.69</b>	<b>0.9187</b>	0.6019

G. Results on Underwater Image Enhancement Task

We conduct underwater enhancement experiments on two real-world benchmarks: UIEB [51] and LSUI [70]. Tab.VII presents the quantitative comparison results, using PSNR and SSIM as reference-based metrics, and UCIQE as a no-reference metric. Compared to the latest methods, SWFormer demonstrates competitive performance, achieving a 0.38 dB PSNR improvement over SFHFormer [43] on the large-scale LSUI dataset. Fig.10 presents the qualitative comparison results. The images restored by our model are closer to the ground truth, excelling in color correction and preserving natural color tones better than other methods in underwater.

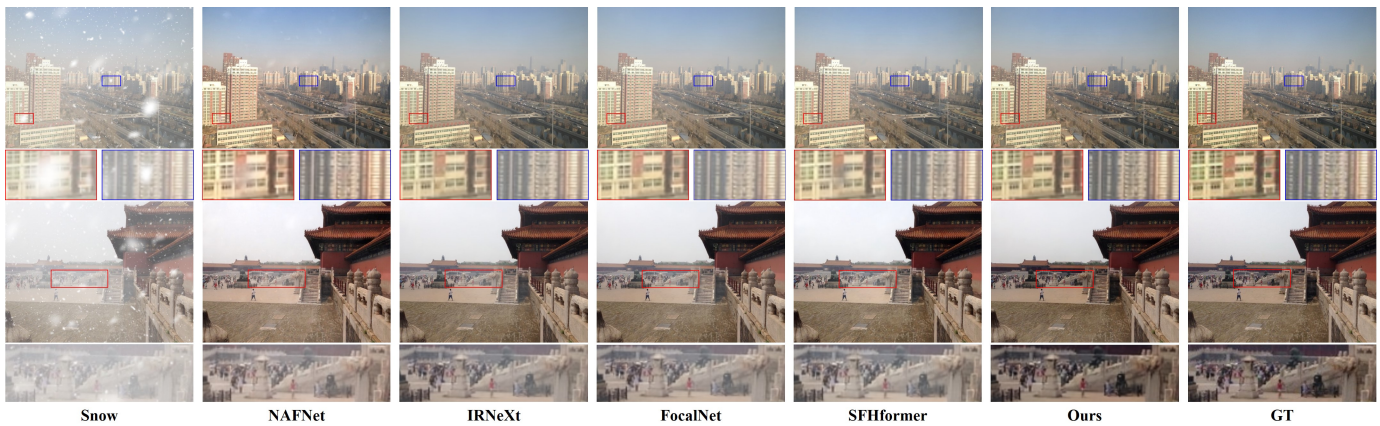


Fig. 11: The quantitative evaluation results on image desnowing.

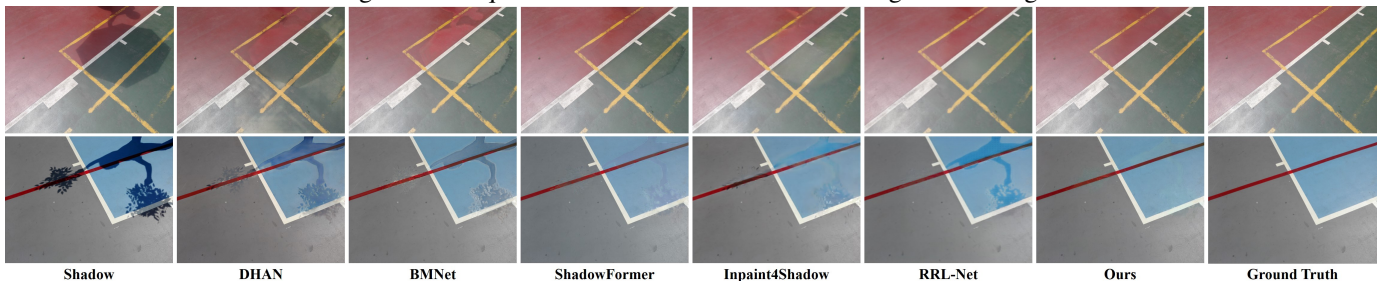


Fig. 12: The quantitative evaluation results on shadow removal.

TABLE VIII: Quantitative evaluations on image desnowing.

Method	CSD [11]		SRRS [10]		Snow100K [62]	
	PSNR $\uparrow$	SSIM $\uparrow$	PSNR $\uparrow$	SSIM $\uparrow$	PSNR $\uparrow$	SSIM $\uparrow$
(CVPR'22)ALL in One [52]	26.31	0.87	24.98	0.88	26.07	0.88
(ECCV'20)JSTASR [10]	27.96	0.88	25.82	0.89	23.12	0.86
(ICCV'21)HDCW-Net [11]	29.06	0.91	27.78	0.92	31.54	0.95
(CVPR'22)TransWeather [88]	31.76	0.93	28.29	0.92	31.82	0.93
(ECCV'22)NAFNet [8]	33.13	0.96	29.72	0.94	32.41	0.95
(ICCV'23)FocalNet [18]	37.18	<b>0.99</b>	31.34	<b>0.98</b>	33.53	<b>0.95</b>
(ICML'23)IRNeXt [19]	37.29	<b>0.99</b>	31.91	<b>0.98</b>	33.61	<b>0.95</b>
(ECCV'24)SFHformer [43]	37.45	<b>0.99</b>	32.39	<b>0.98</b>	33.94	<b>0.95</b>
(Ours)SWFormer-s	36.85	0.98	31.83	<b>0.98</b>	33.82	0.95
(Ours)SWFormer-m	37.43	<b>0.99</b>	32.55	<b>0.98</b>	34.21	<b>0.96</b>
(Ours)SWFormer-l	<b>37.76</b>	<b>0.99</b>	<b>32.81</b>	<b>0.98</b>	<b>34.55</b>	<b>0.96</b>

TABLE IX: Quantitative evaluations on shadow removal.

Method	Shadow Region (S)			Whole Image (ALL)		
	PSNR $\uparrow$	SSIM $\uparrow$	RMSE $\downarrow$	PSNR $\uparrow$	SSIM $\uparrow$	RMSE $\downarrow$
(AAAI'20)DHAN [21]	33.08	0.988	9.49	25.78	0.958	7.74
(CVPR'21)DC-ShadowNet [44]	32.20	0.977	10.83	29.17	0.939	4.70
(CVPR'21)AutoExposure [26]	36.02	0.976	6.67	29.28	0.847	4.28
(CVPR'22)BMNet [112]	38.17	0.991	5.72	34.34	0.974	2.93
(AAAI'23)ShadowFormer [34]	39.67	<b>0.992</b>	5.21	35.46	0.973	2.80
(CVPR'23)ShadowDiffusion [35]	39.82	-	4.90	35.72	-	2.70
(ICCV'23)Inpaint4Shadow [53]	38.46	0.989	5.93	34.14	0.960	3.39
(AAAI'24)RRL-Net [61]	38.04	0.990	5.69	34.96	0.968	2.87
(Ours)SWFormer-s	40.16	<b>0.992</b>	5.04	35.68	<b>0.975</b>	<b>2.69</b>
(Ours)SWFormer-m	<b>40.37</b>	<b>0.992</b>	4.94	<b>35.85</b>	<b>0.976</b>	<b>2.66</b>
(Ours)SWFormer-l	<b>40.45</b>	<b>0.992</b>	<b>4.86</b>	<b>35.79</b>	<b>0.976</b>	<b>2.66</b>

### H. Results on Image Desnowing Task

We conduct snow removal experiments on three widely used large-scale public datasets: CSD [11], SRRS [10] and Snow100K [62]. Tab. VIII presents the quantitative comparison results, where SWFormer consistently surpasses state-of-the-art methods, achieving the best performance in snow removal across all datasets. Notably, it shows an average PSNR improvement of 0.4 dB over SFHFormer [43]. Fig. 11 illustrates the qualitative results. Our model excels at recovering heavily snow-covered areas and effectively eliminating snow from distant views, delivering visually natural and superior outcomes.

### I. Results on Shadow Removal Task

For the shadow removal task, we conduct experiments using the AISTD [47] real-world public dataset. Tab. IX presents the quantitative comparison results, evaluating the restoration performance from two perspectives: the shadow region and the entire image. We use PSNR, SSIM and RMSE as evaluation metrics. Compared to the latest state-of-the-art methods, our proposed SWFormer achieves the highest performance. No-

tably, in the shadow region, our model surpasses the second-best diffusion-based method, ShadowDiffusion [35], with a 0.63 dB PSNR improvement. Fig. 12 illustrates the qualitative comparison results. It is evident that our method provides the most comprehensive shadow removal, delivering the most natural and seamless visual results, without leaving any noticeable traces of shadow removal.

### J. Results on Remote Sensing Cloud Removal Task

For the remote sensing cloud removal task, we conduct experiments using the CUHK-CR [84] real-world public dataset, which includes the light cloud dataset CUHK-CR1 [84] and the heavy cloud dataset CUHK-CR2 [84]. Tab. X presents the quantitative comparison results for cloud removal, where our proposed SWFormer achieves the best PSNR and SSIM metrics, and the second-best LPIPS score. Notably, on the heavy cloud dataset CUHK-CR2, SWFormer shows a 1.14 dB PSNR improvement compared to the latest method, EMRDM [60]. Fig. 13 presents the qualitative comparison results for remote sensing cloud removal. Compared to EMRDM, our method achieves better fidelity in the restored cloud-free images, while

TABLE X: Quantitative evaluations on cloud removal.

Method	CUHK-CR1 [84]			CUHK-CR2 [84]		
	PSNR↑	SSIM↑	LPIPS↓	PSNR↑	SSIM↑	LPIPS↓
(ACCV'22)CVAE [22]	24.252	0.7252	0.1075	22.631	0.6302	0.0489
(ArXiv'23)MemoryNet [108]	26.073	0.7741	0.0315	24.224	0.6838	0.0403
(GRSL'22)MSDA-CR [102]	25.435	0.7483	0.0374	23.755	0.6661	0.0433
(TGRS'24)DE-MemoryNet [84]	26.183	0.7746	0.0290	24.348	0.6843	0.0369
(TGRS'24)DE-MSDA [84]	25.739	0.7592	0.0321	23.968	0.6737	0.0372
(CVPR'25)EMRDM [60]	27.281	0.8007	<b>0.0218</b>	24.594	0.6951	<b>0.0301</b>
(Ours)SWFormer-s	27.213	0.8019	0.0267	25.520	0.7261	0.0351
(Ours)SWFormer-m	<b>27.380</b>	<b>0.8100</b>	<b>0.0241</b>	<b>25.706</b>	<b>0.7417</b>	<b>0.0326</b>
(Ours)SWFormer-l	<b>27.425</b>	<b>0.8126</b>	0.0242	<b>25.737</b>	<b>0.7443</b>	0.0329



Fig. 13: Quantitative evaluation results on cloud removal.

EMRDM tends to introduce more artificial image artifacts, with more distortions or unrealistic details.

### K. Experimental Results on Model Complexity

In Tab.XI, we compare model complexity (Params, FLOPs, MACs) and restoration performance (PSNR, SSIM, LPIPS) across the tasks of deraining, low-light enhancement and defocus deblurring. As shown in Tab.XI(a,b,c), we present the average restoration performance across five deraining datasets (Rain200L [97], Rain200H [97], DDN-Data [27], DID-Data [106], SPA-Data [90]), three low-light datasets (LOL-v1 [93], LOL-v2-real [98], LOL-v2-syn [98]) and two defocus deblurring datasets (DPDD [2], LFDof [79]). Model complexity for deraining and low-light tasks is computed at 256×256 resolution, and for defocus deblurring, at 1280×720 resolution. The results demonstrate that our method achieves an optimal balance between performance and model complexity. Specifically, for rain removal, SWFormer-m uses only 21.4% of the Params and 54.6% of the FLOPs of SFHFormer [43], while outperforming it in both PSNR and SSIM. For defocus blur removal, SWFormer-m uses 58.8% of the Params and 34.2% of the MACs of GGKNet [76], maintaining an advantage in PSNR, SSIM and LPIPS.

### L. Experimental Results on Inference Latency

In Tab.XII, we compare model latency and restoration performance at two different resolutions. In Tab.XII(a), using the low-resolution dataset Rain200L [97] (400×600) at a 256×256 image resolution, SWFormer outperforms the latest methods in both restoration and latency. Notably, SWFormer-s achieves a

2.5× faster inference speed (25.9ms vs. 65.2ms) while improving PSNR by 0.16 dB over SFHFormer [43]. In Tab.XII(b), with the high-resolution dataset 4K-Rain13k [7] (3840×2160) at 1024×1024 resolution, SWFormer-s achieves a 67× faster inference speed (40ms vs. 2682ms) compared to DRSformer [12], while delivering a 1.89 dB PSNR improvement.

TABLE XII: Experimental Results on Model Complexity.

(a) Comparison on 256×256				(b) Comparison on 1024×1024			
Method	Rain200L		Latency	Method	4K-Rain13k		Latency
	PSNR↑	SSIM↑			PSNR↑	SSIM↑	
(CVPR'22)Restormer [103]	40.99	0.9890	77.3ms	(ICCV'21)SPDNet [100]	31.81	0.9223	391ms
(TPAMI'22)IDT [94]	40.74	0.9884	74.8ms	(CVPR'22)Restormer [103]	33.02	0.9335	1145ms
(CVPR'23)DRSformer [12]	41.23	0.9894	176.9ms	(TPAMI'22)IDT [94]	32.91	0.9479	1935ms
(CVPR'24)NeRD-Rain [13]	41.71	0.9903	115.8ms	(CVPR'23)DRSformer [12]	32.96	0.9334	2682ms
(ECCV'24)FADformer [31]	41.80	0.9906	72.1ms	(ICCV'23)UDR-S <sup>2</sup> Former [9]	33.36	0.9458	547ms
(ECCV'24)SFHFormer [43]	41.85	0.9908	65.2ms	(ArXiv'24)UDR-Mixer [7]	34.30	0.9505	77ms
(Ours)SWFormer-s	42.01	0.9908	25.9ms	(Ours)SWFormer-s	34.85	0.9537	40ms
(Ours)SWFormer-m	42.23	0.9913	37.4ms	(Ours)SWFormer-m	35.54	0.9573	51ms
(Ours)SWFormer-l	42.70	0.9922	55.4ms	(Ours)SWFormer-l	35.78	0.9591	82ms

### M. Ablation Studies

To validate the effectiveness of our method, we conduct various ablation experiments on LMIMO and the individual components of SWFormer on the Rain200L [97] dataset.

TABLE XIII: Ablation Study on LMIMO.

No.	SISO	MIMO	LMIMO	PSNR↑	SSIM↑	#Params	#FLOPs	Latency
1	✓			42.11	0.9909	1.83M	38.48G	52.784ms
2		✓		42.55	0.9919	1.90M	39.81G	54.660ms
3			✓	42.70	0.9922	1.91M	40.01G	55.433ms

1) *Ablation Study about Lossless Multi-Input Multi-Output:* Tab.XIII presents the comparisons under different inter-block structures (SISO, MIMO, LMIMO), showing that our LMIMO framework achieves superior performance. Specifically, compared to SISO, LMIMO achieves a 0.59dB PSNR improvement at the cost of 0.08M parameters, 1.53G computation and 2.649ms inference time. Compared to MIMO, LMIMO achieves a 0.15dB PSNR improvement with a cost of 0.01M parameters, 0.20G computation and 0.773ms inference time.

TABLE XIV: Ablation Study on Individual Components.

Individual Component	Spatial branch	✓		✓	✓	✓	✓	✓	✓		
	Wavelet branch		✓	✓	✓	✓	✓	✓	✓		
	Fourier branch			✓	✓	✓	✓	✓	✓		
	Spatial loss	✓		✓	✓	✓	✓	✓	✓		
	Wavelet loss		✓	✓	✓	✓	✓	✓	✓		
	Fourier loss			✓	✓	✓	✓	✓	✓		
Metric	DFFN [92]							✓			
	GDFN [103]							✓			
	MCFN [43]								✓		
	MSFN	✓	✓	✓	✓	✓	✓		✓		
Metric	PSNR↑	42.10	42.08	42.43	42.15	42.53	42.60	42.63	42.62	42.66	42.70
	SSIM↑	0.9910	0.9909	0.9918	0.9912	0.9919	0.9920	0.9921	0.9920	0.9921	0.9922

2) *Ablation Study about Individual Components:* Tab.XIV presents the ablation results for SWFormer's individual components, focusing on the Token Mixer and FFN at the intra-block level. To ensure fairness, we fine-tune each configuration to match model parameters and computational cost.

TABLE XI: Experimental Results on Model Performance and Complexity Balance.

(a) Comparison on Deraining				(b) Comparison on Low-light				(c) Comparison on Deblurring							
Method	Deraining		Overhead		Method	Low-light		Overhead		Method	Defocus blur			Overhead	
	PSNR↑	SSIM↑	#Params	#FLOPs		PSNR↑	SSIM↑	#Params	#FLOPs		PSNR↑	SSIM↑	LPIPS↓	#Params	#MACs
(CVPR'22)Uformer [92]	37.22	0.9609	20.60M	41.09G	(CVPR'22)Restormer [103]	23.45	0.841	26.10M	141.0G	(CVPR'21)KPAC [82]	27.082	0.816	0.200	2.06M	98.5B
(CVPR'22)Restormer [103]	38.09	0.9670	26.10M	141.0G	(ECCV'22)LEDNet [110]	24.16	0.868	7.07M	35.92G	(CVPR'21)JFANet [48]	27.578	0.831	0.186	10.48M	362.9B
(TPAMI'22)IDT [94]	37.78	0.9666	16.39M	58.44G	(CVPR'22)SNR-Net [95]	25.33	0.880	4.01M	26.35G	(NIPS'21)GKNet [74]	27.275	0.828	0.195	1.47M	147.8B
(CVPR'23)DRSformer [12]	38.33	0.9676	33.70M	242.9G	(AAAI'23)LLFormer [89]	24.62	0.848	24.55M	22.52G	(CVPR'22)DRBNet [80]	27.869	0.838	0.201	11.7M	346.6B
(CVPR'24)NeRD-Rain [13]	38.73	0.9694	22.89M	156.3G	(ICCV'23)RetinexFormer [6]	26.24	0.877	1.61M	15.57G	(CVPR'23)NRKNet [75]	28.295	0.847	0.179	6.09M	552.8B
(ECCV'24)FADformer [31]	38.68	0.9692	6.96M	48.51G	(ECCV'24)SFHFormer [43]	26.38	0.894	1.04M	7.75G	(ECCV'24)SFHFormer [43]	28.371	0.847	0.184	7.76M	267.5B
(ECCV'24)SFHFormer [43]	38.82	0.9690	7.63M	50.59G	(CVPR'25)CIDNet [96]	26.35	0.899	1.88M	7.57G	(TPAMI'24)GGKNet [76]	28.412	0.848	0.185	5.93M	518.9B
(Ours)SWFormer-s	38.57	0.9680	0.95M	19.86G	(Ours)SWFormer-s	26.59	0.889	1.22M	7.00G	(Ours)SWFormer-s	28.345	0.847	0.181	3.10M	114.2B
(Ours)SWFormer-m	38.87	0.9695	1.63M	27.65G	(Ours)SWFormer-m	26.92	0.893	1.47M	9.41G	(Ours)SWFormer-m	28.569	0.855	0.180	3.49M	145.2B
(Ours)SWFormer-l	39.23	0.9716	1.91M	40.01G	(Ours)SWFormer-l	27.28	0.906	1.54M	11.97G	(Ours)SWFormer-l	28.745	0.859	0.177	3.60M	177.6B

For the Spatial-Wavelet-Fourier Mixer, we assess the contribution of each domain to feature extraction. The results reveal that multi-domain learning enhances feature extraction across multi-receptive fields, with the Fourier domain having the greatest impact, followed by the equally significant Spatial and Wavelet domains. In FFN, we compare our MSFN with MCFN [43], GDFN [103] and DFFN [92], and find that MSFN yields better performance.

TABLE XV: Ablation Study on Fourier Operation.

No.	FDC [43]	Gate Filter	PSNR $\uparrow$	SSIM $\uparrow$	#Params	#FLOPs	Latency
1	✓		42.75	0.9923	1.89M	39.12G	73.181ms
2		✓	42.70	0.9922	1.91M	40.01G	55.433ms

3) *Ablation Study about Fourier Operation:* Tab.XV compares the Gate Filter in the Fourier branch with the frequency dynamic convolution (FDC) from the conference version [43]. While FDC achieves slightly better performance in PSNR, parameters and computational cost (0.05 dB, 0.02 M, 0.89 G), its inference time is significantly longer, being 1.32 times ours, with an additional 17.748 ms. Given this trade-off, we choose the Gate Filter, which offers a slight performance cost in exchange for a substantial reduction in latency.

## V. CONCLUSION

In this work, we uncover a novel restoration prior from a Spatial-Wavelet-Fourier perspective, offering new insights for efficient and precise feature extraction. Guided by this, we propose SWFormer, an efficient Transformer-like backbone that integrates multi-domain learning to address image restoration. At the inter-block level, we introduce a Lossless Multi-Input Multi-Output framework, enabling dynamic outputs at varying sizes and restoration enhancement with minimal computational overhead. At the intra-block level, we retain the Transformer architecture but modify the Token Mixer and Feed-Forward Network. Specifically, in the Token Mixer, we replaces self-attention with a tri-branch structure for local-region-global modeling, reducing model complexity. In the FFN, we implement multi-scale learning to aggregate features across different domains and resolutions. We evaluate SWFormer through extensive experiments on 26 benchmarks across 10 restoration tasks, including dehazing, desnowing, rain streak/raindrop removal, cloud removal, motion blur, defocus blur, shadow removal, underwater enhancement and low-light enhancement. The results show that SWFormer achieves SOTA performance on most datasets, balancing performance, model size, computational cost and inference latency effectively.

## REFERENCES

- [1] Abuolaim, A., Afifi, M., Brown, M.S.: Improving single-image defocus deblurring: How dual-pixel images help through multi-task learning. In: Proceedings of the IEEE/CVF Winter Conference on Applications of Computer Vision. pp. 1231–1239 (2022)
- [2] Abuolaim, A., Brown, M.S.: Defocus deblurring using dual-pixel data. In: Eur. Conf. Comput. Vis. pp. 111–126. Springer (2020)
- [3] Ancuti, C.O., Ancuti, C., Sbert, M., Timofte, R.: Dense-haze: A benchmark for image dehazing with dense-haze and haze-free images. In: 2019 IEEE international conference on image processing (ICIP). pp. 1014–1018. IEEE (2019)
- [4] Ancuti, C.O., Ancuti, C., Timofte, R.: Nh-haze: An image dehazing benchmark with non-homogeneous hazy and haze-free images. In: Proceedings of the IEEE/CVF conference on computer vision and pattern recognition workshops. pp. 444–445 (2020)
- [5] Ancuti, C.O., Ancuti, C., Timofte, R., De Vleeschouwer, C.: O-haze: a dehazing benchmark with real hazy and haze-free outdoor images. In: Proceedings of the IEEE conference on computer vision and pattern recognition workshops. pp. 754–762 (2018)
- [6] Cai, Y., Bian, H., Lin, J., Wang, H., Timofte, R., Zhang, Y.: Retinex-former: One-stage retinex-based transformer for low-light image enhancement. arXiv preprint arXiv:2303.06705 (2023)
- [7] Chen, H., Chen, X., Wu, C., Zheng, Z., Pan, J., Fu, X.: Towards ultra-high-definition image deraining: A benchmark and an efficient method. arXiv preprint arXiv:2405.17074 (2024)
- [8] Chen, L., Chu, X., Zhang, X., Sun, J.: Simple baselines for image restoration. In: Eur. Conf. Comput. Vis. pp. 17–33. Springer (2022)
- [9] Chen, S., Ye, T., Bai, J., Chen, E., Shi, J., Zhu, L.: Sparse sampling transformer with uncertainty-driven ranking for unified removal of raindrops and rain streaks. In: Int. Conf. Comput. Vis. pp. 13106–13117 (2023)
- [10] Chen, W.T., Fang, H.Y., Ding, J.J., Tsai, C.C., Kuo, S.Y.: Jstasr: Joint size and transparency-aware snow removal algorithm based on modified partial convolution and veiling effect removal. In: Eur. Conf. Comput. Vis. pp. 754–770. Springer (2020)
- [11] Chen, W.T., Fang, H.Y., Hsieh, C.L., Tsai, C.C., Chen, I., Ding, J.J., Kuo, S.Y., et al.: All snow removed: Single image desnowing algorithm using hierarchical dual-tree complex wavelet representation and contradict channel loss. In: Int. Conf. Comput. Vis. pp. 4196–4205 (2021)
- [12] Chen, X., Li, H., Li, M., Pan, J.: Learning a sparse transformer network for effective image deraining. In: IEEE Conf. Comput. Vis. Pattern Recog. pp. 5896–5905 (2023)
- [13] Chen, X., Pan, J., Dong, J.: Bidirectional multi-scale implicit neural representations for image deraining. In: IEEE Conf. Comput. Vis. Pattern Recog. pp. 25627–25636 (2024)
- [14] Chen, X., Pan, J., Lu, J., Fan, Z., Li, H.: Hybrid cnn-transformer feature fusion for single image deraining. In: Proceedings of the AAAI conference on artificial intelligence. vol. 37, pp. 378–386 (2023)
- [15] Chen, X., Li, Z., Pu, Y., Liu, Y., Zhou, J., Qiao, Y., Dong, C.: A comparative study of image restoration networks for general backbone network design. In: Eur. Conf. Comput. Vis. pp. 74–91. Springer (2024)
- [16] Cho, S.J., Ji, S.W., Hong, J.P., Jung, S.W., Ko, S.J.: Rethinking coarse-to-fine approach in single image deblurring. In: Int. Conf. Comput. Vis. pp. 4641–4650 (2021)
- [17] Chu, X., Chen, L., Chen, C., Lu, X.: Improving image restoration by revisiting global information aggregation. In: Eur. Conf. Comput. Vis. pp. 53–71. Springer (2022)
- [18] Cui, Y., Ren, W., Cao, X., Knoll, A.: Focal network for image restoration. In: Int. Conf. Comput. Vis. pp. 13001–13011 (2023)
- [19] Cui, Y., Ren, W., Yang, S., Cao, X., Knoll, A.: Irnext: Rethinking convolutional network design for image restoration. In: Int. Conf. Mach. Learn. (2023)
- [20] Cui, Y., Tao, Y., Bing, Z., Ren, W., Gao, X., Cao, X., Huang, K., Knoll, A.: Selective frequency network for image restoration. In: Int. Conf. Learn. Represent. (2022)
- [21] Cun, X., Pun, C.M., Shi, C.: Towards ghost-free shadow removal via dual hierarchical aggregation network and shadow matting gan. In: Proceedings of the AAAI conference on artificial intelligence. vol. 34, pp. 10680–10687 (2020)
- [22] Ding, H., Zi, Y., Xie, F.: Uncertainty-based thin cloud removal network via conditional variational autoencoders. In: Proceedings of the Asian Conference on Computer Vision. pp. 469–485 (2022)
- [23] Dong, H., Pan, J., Xiang, L., Hu, Z., Zhang, X., Wang, F., Yang, M.H.: Multi-scale boosted dehazing network with dense feature fusion. In: IEEE Conf. Comput. Vis. Pattern Recog. pp. 2157–2167 (2020)
- [24] Dosovitskiy, A., Beyer, L., Kolesnikov, A., Weissenborn, D., Zhai, X., Unterthiner, T., Dehghani, M., Minderer, M., Heigold, G., Gelly, S., et al.: An image is worth 16x16 words: Transformers for image recognition at scale. In: Int. Conf. Learn. Represent. (2020)
- [25] Engin, D., Genç, A., Kemal Ekenel, H.: Cycle-dehaze: Enhanced cyclegan for single image dehazing. In: Proceedings of the IEEE conference on computer vision and pattern recognition workshops. pp. 825–833 (2018)
- [26] Fu, L., Zhou, C., Guo, Q., Juefei-Xu, F., Yu, H., Feng, W., Liu, Y., Wang, S.: Auto-exposure fusion for single-image shadow removal. In: IEEE Conf. Comput. Vis. Pattern Recog. pp. 10571–10580 (2021)

- [27] Fu, X., Huang, J., Zeng, D., Huang, Y., Ding, X., Paisley, J.: Removing rain from single images via a deep detail network. In: IEEE Conf. Comput. Vis. Pattern Recog. pp. 3855–3863 (2017)
- [28] Fu, X., Qi, Q., Zha, Z.J., Zhu, Y., Ding, X.: Rain streak removal via dual graph convolutional network. In: Proceedings of the AAAI Conference on Artificial Intelligence. vol. 35, pp. 1352–1360 (2021)
- [29] Fu, Z., Wang, W., Huang, Y., Ding, X., Ma, K.K.: Uncertainty inspired underwater image enhancement. In: Eur. Conf. Comput. Vis. pp. 465–482. Springer (2022)
- [30] Fu, Z., Yang, Y., Tu, X., Huang, Y., Ding, X., Ma, K.K.: Learning a simple low-light image enhancer from paired low-light instances. In: IEEE Conf. Comput. Vis. Pattern Recog. pp. 22252–22261 (2023)
- [31] Gao, N., Jiang, X., Zhang, X., Deng, Y.: Efficient frequency-domain image deraining with contrastive regularization. In: Eur. Conf. Comput. Vis. pp. 240–257. Springer (2024)
- [32] Guo, C.L., Yan, Q., Anwar, S., Cong, R., Ren, W., Li, C.: Image dehazing transformer with transmission-aware 3d position embedding. In: IEEE Conf. Comput. Vis. Pattern Recog. pp. 5812–5820 (2022)
- [33] Guo, H., Li, J., Dai, T., Ouyang, Z., Ren, X., Xia, S.T.: Mambair: A simple baseline for image restoration with state-space model. In: Eur. Conf. Comput. Vis. pp. 222–241. Springer (2024)
- [34] Guo, L., Huang, S., Liu, D., Cheng, H., Wen, B.: Shadowformer: global context helps shadow removal. In: Proceedings of the AAAI conference on artificial intelligence. vol. 37, pp. 710–718 (2023)
- [35] Guo, L., Wang, C., Yang, W., Huang, S., Wang, Y., Pfister, H., Wen, B.: Shadowdiffusion: When degradation prior meets diffusion model for shadow removal. In: IEEE Conf. Comput. Vis. Pattern Recog. pp. 14049–14058 (2023)
- [36] He, K., Sun, J., Tang, X.: Single image haze removal using dark channel prior. IEEE Trans. Pattern Anal. Mach. Intell. **33**(12), 2341–2353 (2010)
- [37] He, K., Zhang, X., Ren, S., Sun, J.: Deep residual learning for image recognition. In: IEEE Conf. Comput. Vis. Pattern Recog. pp. 770–778 (2016)
- [38] Huang, C.K., Nien, H.H.: Multi chaotic systems based pixel shuffle for image encryption. Optics communications **282**(11), 2123–2127 (2009)
- [39] Huang, G., Liu, Z., Van Der Maaten, L., Weinberger, K.Q.: Densely connected convolutional networks. In: IEEE Conf. Comput. Vis. Pattern Recog. pp. 4700–4708 (2017)
- [40] Huang, S.C., Le, T.H., Jaw, D.W.: Dsnnet: Joint semantic learning for object detection in inclement weather conditions. IEEE Trans. Pattern Anal. Mach. Intell. **43**(8), 2623–2633 (2020)
- [41] Huo, F., Li, B., Zhu, X.: Efficient wavelet boost learning-based multi-stage progressive refinement network for underwater image enhancement. In: Int. Conf. Comput. Vis. pp. 1944–1952 (2021)
- [42] Jiang, X., Dou, H., Fu, C., Dai, B., Xu, T., Deng, Y.: Boosting supervised dehazing methods via bi-level patch reweighting. In: Eur. Conf. Comput. Vis. pp. 57–73. Springer (2022)
- [43] Jiang, X., Zhang, X., Gao, N., Deng, Y.: When fast fourier transform meets transformer for image restoration. In: Eur. Conf. Comput. Vis. pp. 381–402. Springer (2024)
- [44] Jin, Y., Sharma, A., Tan, R.T.: Dc-shadownet: Single-image hard and soft shadow removal using unsupervised domain-classifier guided network. In: Int. Conf. Comput. Vis. pp. 5027–5036 (2021)
- [45] Kong, L., Dong, J., Ge, J., Li, M., Pan, J.: Efficient frequency domain-based transformers for high-quality image deblurring. In: IEEE Conf. Comput. Vis. Pattern Recog. pp. 5886–5895 (2023)
- [46] Land, E.H., McCann, J.J.: Lightness and retinex theory. Journal of the Optical society of America **61**(1), 1–11 (1971)
- [47] Le, H., Samaras, D.: Shadow removal via shadow image decomposition. In: Int. Conf. Comput. Vis. pp. 8578–8587 (2019)
- [48] Lee, J., Son, H., Rim, J., Cho, S., Lee, S.: Iterative filter adaptive network for single image defocus deblurring. In: IEEE Conf. Comput. Vis. Pattern Recog. pp. 2034–2042 (2021)
- [49] Li, B., Peng, X., Wang, Z., Xu, J., Feng, D.: Aod-net: All-in-one dehazing network. In: Proceedings of the IEEE international conference on computer vision. pp. 4770–4778 (2017)
- [50] Li, B., Ren, W., Fu, D., Tao, D., Feng, D., Zeng, W., Wang, Z.: Benchmarking single-image dehazing and beyond. IEEE Trans. Image Process. **28**(1), 492–505 (2018)
- [51] Li, C., Guo, C., Ren, W., Cong, R., Hou, J., Kwong, S., Tao, D.: An underwater image enhancement benchmark dataset and beyond. IEEE Trans. Image Process. **29**, 4376–4389 (2019)
- [52] Li, R., Tan, R.T., Cheong, L.F.: All in one bad weather removal using architectural search. In: IEEE Conf. Comput. Vis. Pattern Recog. pp. 3175–3185 (2020)
- [53] Li, X., Guo, Q., Abdelfattah, R., Lin, D., Feng, W., Tsang, I., Wang, S.: Leveraging inpainting for single-image shadow removal. In: Int. Conf. Comput. Vis. pp. 13055–13064 (2023)
- [54] Li, Y., Fan, Y., Xiang, X., Demandolx, D., Ranjan, R., Timofte, R., Van Gool, L.: Efficient and explicit modelling of image hierarchies for image restoration. In: IEEE Conf. Comput. Vis. Pattern Recog. pp. 18278–18289 (2023)
- [55] Lin, T.Y., Dollár, P., Girshick, R., He, K., Hariharan, B., Belongie, S.: Feature pyramid networks for object detection. In: IEEE Conf. Comput. Vis. Pattern Recog. pp. 2117–2125 (2017)
- [56] Liu, C., Wang, X., Xu, X., Tian, R., Li, S., Qian, X., Yang, M.H.: Motion-adaptive separable collaborative filters for blind motion deblurring. In: IEEE Conf. Comput. Vis. Pattern Recog. pp. 25595–25605 (2024)
- [57] Liu, R., Ma, L., Zhang, J., Fan, X., Luo, Z.: Retinex-inspired unrolling with cooperative prior architecture search for low-light image enhancement. In: IEEE Conf. Comput. Vis. Pattern Recog. pp. 10561–10570 (2021)
- [58] Liu, X., Ma, Y., Shi, Z., Chen, J.: Griddehazenet: Attention-based multi-scale network for image dehazing. In: Int. Conf. Comput. Vis. pp. 7314–7323 (2019)
- [59] Liu, X., Suganuma, M., Sun, Z., Okatani, T.: Dual residual networks leveraging the potential of paired operations for image restoration. In: IEEE Conf. Comput. Vis. Pattern Recog. pp. 7007–7016 (2019)
- [60] Liu, Y., Li, W., Guan, J., Zhou, S., Zhang, Y.: Effective cloud removal for remote sensing images by an improved mean-reverting denoising model with elucidated design space. arXiv preprint arXiv:2503.23717 (2025)
- [61] Liu, Y., Ke, Z., Xu, K., Liu, F., Wang, Z., Lau, R.W.: Recasting regional lighting for shadow removal. In: Proceedings of the AAAI Conference on Artificial Intelligence. vol. 38, pp. 3810–3818 (2024)
- [62] Liu, Y.F., Jaw, D.W., Huang, S.C., Hwang, J.N.: Desnownet: Context-aware deep network for snow removal. IEEE Trans. Image Process. **27**(6), 3064–3073 (2018)
- [63] Liu, Z., Lin, Y., Cao, Y., Hu, H., Wei, Y., Zhang, Z., Lin, S., Guo, B.: Swin transformer: Hierarchical vision transformer using shifted windows. In: Int. Conf. Comput. Vis. pp. 10012–10022 (2021)
- [64] Loshchilov, I., Hutter, F.: Sgdr: Stochastic gradient descent with warm restarts. arXiv preprint arXiv:1608.03983 (2016)
- [65] Loshchilov, I., Hutter, F.: Decoupled weight decay regularization. arXiv preprint arXiv:1711.05101 (2017)
- [66] Nah, S., Hyun Kim, T., Mu Lee, K.: Deep multi-scale convolutional neural network for dynamic scene deblurring. In: IEEE Conf. Comput. Vis. Pattern Recog. pp. 3883–3891 (2017)
- [67] Naik, A., Swarnakar, A., Mittal, K.: Shallow-uwnet: Compressed model for underwater image enhancement (student abstract). In: Proceedings of the AAAI Conference on Artificial Intelligence. vol. 35, pp. 15853–15854 (2021)
- [68] Özdenizci, O., Legenstein, R.: Restoring vision in adverse weather conditions with patch-based denoising diffusion models. IEEE Trans. Pattern Anal. Mach. Intell. (2023)
- [69] Paszke, A., Gross, S., Massa, F., Lerer, A., Bradbury, J., Chanan, G., Killeen, T., Lin, Z., Gimelshein, N., Antiga, L., et al.: Pytorch: An imperative style, high-performance deep learning library. Adv. Neural Inform. Process. Syst. **32** (2019)
- [70] Peng, L., Zhu, C., Bian, L.: U-shape transformer for underwater image enhancement. IEEE Trans. Image Process. (2023)
- [71] Qian, R., Tan, R.T., Yang, W., Su, J., Liu, J.: Attentive generative adversarial network for raindrop removal from a single image. In: IEEE Conf. Comput. Vis. Pattern Recog. pp. 2482–2491 (2018)
- [72] Qin, X., Wang, Z., Bai, Y., Xie, X., Jia, H.: Ffa-net: Feature fusion attention network for single image dehazing. In: Proceedings of the AAAI conference on artificial intelligence. vol. 34, pp. 11908–11915 (2020)
- [73] Qiu, Y., Zhang, K., Wang, C., Luo, W., Li, H., Jin, Z.: Mb-taylorformer: Multi-branch efficient transformer expanded by taylor formula for image dehazing. In: Int. Conf. Comput. Vis. pp. 12802–12813 (2023)
- [74] Quan, Y., Wu, Z., Ji, H.: Gaussian kernel mixture network for single image defocus deblurring. Adv. Neural Inform. Process. Syst. **34**, 20812–20824 (2021)
- [75] Quan, Y., Wu, Z., Ji, H.: Neumann network with recursive kernels for single image defocus deblurring. In: IEEE Conf. Comput. Vis. Pattern Recog. pp. 5754–5763 (2023)
- [76] Quan, Y., Wu, Z., Xu, R., Ji, H.: Deep single image defocus deblurring via gaussian kernel mixture learning. IEEE Trans. Pattern Anal. Mach. Intell. (2024)

- [77] Ren, M., Delbraccio, M., Talebi, H., Gerig, G., Milanfar, P.: Multiscale structure guided diffusion for image deblurring. In: *Int. Conf. Comput. Vis.* pp. 10721–10733 (2023)
- [78] Ren, T., Xu, H., Jiang, G., Yu, M., Zhang, X., Wang, B., Luo, T.: Reinforced swin-convs transformer for simultaneous underwater sensing scene image enhancement and super-resolution. *IEEE Transactions on Geoscience and Remote Sensing* **60**, 1–16 (2022)
- [79] Ruan, L., Chen, B., Li, J., Lam, M.L.: Aifnet: All-in-focus image restoration network using a light field-based dataset. *IEEE Transactions on Computational Imaging* **7**, 675–688 (2021)
- [80] Ruan, L., Chen, B., Li, J., Lam, M.: Learning to deblur using light field generated and real defocus images. In: *IEEE Conf. Comput. Vis. Pattern Recog.* pp. 16304–16313 (2022)
- [81] Shen, Z., Wang, W., Lu, X., Shen, J., Ling, H., Xu, T., Shao, L.: Human-aware motion deblurring. In: *Int. Conf. Comput. Vis.* pp. 5572–5581 (2019)
- [82] Son, H., Lee, J., Cho, S., Lee, S.: Single image defocus deblurring using kernel-sharing parallel atrous convolutions. In: *Int. Conf. Comput. Vis.* pp. 2642–2650 (2021)
- [83] Song, Y., He, Z., Qian, H., Du, X.: Vision transformers for single image dehazing. *IEEE Trans. Image Process.* **32**, 1927–1941 (2023)
- [84] Sui, J., Ma, Y., Yang, W., Zhang, X., Pun, M.O., Liu, J.: Diffusion enhancement for cloud removal in ultra-resolution remote sensing imagery. *IEEE Transactions on Geoscience and Remote Sensing* (2024)
- [85] Szegedy, C., Vanhoucke, V., Ioffe, S., Shlens, J., Wojna, Z.: Rethinking the inception architecture for computer vision. In: *IEEE Conf. Comput. Vis. Pattern Recog.* pp. 2818–2826 (2016)
- [86] Tsai, F.J., Peng, Y.T., Lin, Y.Y., Tsai, C.C., Lin, C.W.: Stripformer: Strip transformer for fast image deblurring. In: *Eur. Conf. Comput. Vis.* pp. 146–162. Springer (2022)
- [87] Tu, Z., Talebi, H., Zhang, H., Yang, F., Milanfar, P., Bovik, A., Li, Y.: Maxim: Multi-axis mlp for image processing. In: *IEEE Conf. Comput. Vis. Pattern Recog.* pp. 5769–5780 (2022)
- [88] Valanarasu, J.M.J., Yasarla, R., Patel, V.M.: Transweather: Transformer-based restoration of images degraded by adverse weather conditions. In: *IEEE Conf. Comput. Vis. Pattern Recog.* pp. 2353–2363 (2022)
- [89] Wang, T., Zhang, K., Shen, T., Luo, W., Stenger, B., Lu, T.: Ultra-high-definition low-light image enhancement: A benchmark and transformer-based method. In: *Proceedings of the AAAI conference on artificial intelligence.* vol. 37, pp. 2654–2662 (2023)
- [90] Wang, T., Yang, X., Xu, K., Chen, S., Zhang, Q., Lau, R.W.: Spatial attentive single-image deraining with a high quality real rain dataset. In: *IEEE Conf. Comput. Vis. Pattern Recog.* pp. 12270–12279 (2019)
- [91] Wang, Y., Wan, R., Yang, W., Li, H., Chau, L.P., Kot, A.: Low-light image enhancement with normalizing flow. In: *Proceedings of the AAAI conference on artificial intelligence.* vol. 36, pp. 2604–2612 (2022)
- [92] Wang, Z., Cun, X., Bao, J., Zhou, W., Liu, J., Li, H.: Uformer: A general u-shaped transformer for image restoration. In: *IEEE Conf. Comput. Vis. Pattern Recog.* pp. 17683–17693 (2022)
- [93] Wei, C., Wang, W., Yang, W., Liu, J.: Deep retinex decomposition for low-light enhancement. *arXiv preprint arXiv:1808.04560* (2018)
- [94] Xiao, J., Fu, X., Liu, A., Wu, F., Zha, Z.J.: Image de-raining transformer. *IEEE Trans. Pattern Anal. Mach. Intell.* (2022)
- [95] Xu, X., Wang, R., Fu, C.W., Jia, J.: Snr-aware low-light image enhancement. In: *IEEE Conf. Comput. Vis. Pattern Recog.* pp. 17714–17724 (2022)
- [96] Yan, Q., Feng, Y., Zhang, C., Pang, G., Shi, K., Wu, P., Dong, W., Sun, J., Zhang, Y.: Hvi: A new color space for low-light image enhancement. *arXiv preprint arXiv:2502.20272* (2025)
- [97] Yang, W., Tan, R.T., Feng, J., Liu, J., Guo, Z., Yan, S.: Deep joint rain detection and removal from a single image. In: *IEEE Conf. Comput. Vis. Pattern Recog.* pp. 1357–1366 (2017)
- [98] Yang, W., Wang, W., Huang, H., Wang, S., Liu, J.: Sparse gradient regularized deep retinex network for robust low-light image enhancement. *IEEE Trans. Image Process.* **30**, 2072–2086 (2021)
- [99] Ye, T., Zhang, Y., Jiang, M., Chen, L., Liu, Y., Chen, S., Chen, E.: Perceiving and modeling density for image dehazing. In: *Eur. Conf. Comput. Vis.* pp. 130–145. Springer (2022)
- [100] Yi, Q., Li, J., Dai, Q., Fang, F., Zhang, G., Zeng, T.: Structure-preserving deraining with residue channel prior guidance. In: *Int. Conf. Comput. Vis.* pp. 4238–4247 (2021)
- [101] Yu, W., Luo, M., Zhou, P., Si, C., Zhou, Y., Wang, X., Feng, J., Yan, S.: Metaformer is actually what you need for vision. In: *IEEE Conf. Comput. Vis. Pattern Recog.* pp. 10819–10829 (2022)
- [102] Yu, W., Zhang, X., Pun, M.O.: Cloud removal in optical remote sensing imagery using multiscale distortion-aware networks. *IEEE Geoscience and Remote Sensing Letters* **19**, 1–5 (2022)
- [103] Zamir, S.W., Arora, A., Khan, S., Hayat, M., Khan, F.S., Yang, M.H.: Restormer: Efficient transformer for high-resolution image restoration. In: *IEEE Conf. Comput. Vis. Pattern Recog.* pp. 5728–5739 (2022)
- [104] Zamir, S.W., Arora, A., Khan, S., Hayat, M., Khan, F.S., Yang, M.H., Shao, L.: Multi-stage progressive image restoration. In: *IEEE Conf. Comput. Vis. Pattern Recog.* pp. 14821–14831 (2021)
- [105] Zeng, H., Cai, J., Li, L., Cao, Z., Zhang, L.: Learning image-adaptive 3d lookup tables for high performance photo enhancement in real-time. *IEEE Trans. Pattern Anal. Mach. Intell.* **44**(4), 2058–2073 (2020)
- [106] Zhang, H., Patel, V.M.: Density-aware single image de-raining using a multi-stream dense network. In: *IEEE Conf. Comput. Vis. Pattern Recog.* pp. 695–704 (2018)
- [107] Zhang, H., Xiao, L., Cao, X., Foroosh, H.: Multiple adverse weather conditions adaptation for object detection via causal intervention. *IEEE Trans. Pattern Anal. Mach. Intell.* **46**(3), 1742–1756 (2022)
- [108] Zhang, X.F., Gu, C.C., Zhu, S.Y.: Memory augment is all you need for image restoration. *arXiv preprint arXiv:2309.01377* (2023)
- [109] Zheng, Y., Zhan, J., He, S., Dong, J., Du, Y.: Curricular contrastive regularization for physics-aware single image dehazing. In: *IEEE Conf. Comput. Vis. Pattern Recog.* pp. 5785–5794 (2023)
- [110] Zhou, S., Li, C., Change Loy, C.: Lednet: Joint low-light enhancement and deblurring in the dark. In: *Eur. Conf. Comput. Vis.* pp. 573–589. Springer (2022)
- [111] Zhou, S., Chen, D., Pan, J., Shi, J., Yang, J.: Adapt or perish: Adaptive sparse transformer with attentive feature refinement for image restoration. In: *IEEE Conf. Comput. Vis. Pattern Recog.* pp. 2952–2963 (2024)
- [112] Zhu, Y., Huang, J., Fu, X., Zhao, F., Sun, Q., Zha, Z.J.: Bijective mapping network for shadow removal. In: *IEEE Conf. Comput. Vis. Pattern Recog.* pp. 5627–5636 (2022)



**Xingyu Jiang** received the B.S. degree in aircraft control and information engineering from the Image Processing Center, School of Astronautics, Beihang University, Beijing, China, in 2021, where he is currently working toward the Ph.D. degree in control science and engineering. His research interests include low-level computer vision, reinforcement learning and large language models.



**Ning Gao** received the B.S. degree in aircraft control and information engineering from the Image Processing Center, School of Astronautics, Beihang University, Beijing, China, in 2024, where he is currently working toward the Master degree in control science and engineering. His research interests include machine learning, computer vision, reinforcement learning and large language models.



**Xiuhui Zhang** received the B.S. degree in Guiding, Navigation and Control from School of Astronautics, Beihang University, Beijing, China, in 2023. He is currently working toward the Ph.D. degree in artificial intelligence in Institute of Artificial Intelligence, Beihang University, Beijing, China. His research interests include machine learning and its application in interdisciplinary domains.



**Hongkun Dou** received the B.S. degree in aircraft control and information engineering from the Image Processing Center, School of Astronautics, Beihang University, Beijing, China, in 2021, where he is currently working toward the Ph.D. degree in control science and engineering. His research interests include machine learning and its application in interdisciplinary domains.



**Shaowen Fu** graduated from Harbin Institute of Technology in China in 2008, with Ph.D in control science and engineering. His research interests include control theory and navigation.



**Xiaoqing Zhong** received the B.S. and Ph.D. degrees in control science and technology from the Harbin Institute of Technology, Harbin, China, in 2005 and 2010, respectively. He is currently a Research Fellow of the China Academy of Space Technology, Beijing, China. His research interests include spacecraft system engineering and satellite communication.



**Hongjue Li** received the Ph.D. degree in aerospace engineering from Beihang University, Beijing, China, in 2020. He is currently working as an associate professor with the School of Astronautics, Beihang University. His research interests include guidance and control, trajectory optimization, deep learning, and real-time optimal control with AI.



**Yue Deng** (Senior Member, IEEE) received the Ph.D. degree in control science and engineering from the Department of Automation, Tsinghua University, Beijing, China, in 2013. He is currently a Professor with the School of Astronautics, Beihang University, Beijing, China. His research interests include machine learning, signal processing, and computational biology. He is an Associate Editor of *IEEE Transactions on Neural Networks and Learning Systems* and *IEEE Signal Processing Letters*.